Title

Carboxylate-Capped Analogues of Ru265 Are MCU Inhibitor Prodrugs.

Journal

Inorganic Chemistry, 61(43)

Authors

Bigham, Nicholas

Huang, Zhouyang

Spivey, Jesse

et al.

Publication Date

2022-10-31

DOI

10.1021/acs.inorgchem.2c02930

Peer reviewed

Published in final edited form as:

Inorg Chem. 2022 October 31; 61(43): 17299–17312. doi:10.1021/acs.inorgchem.2c02930.

Carboxylate-Capped Analogues of Ru265 are MCU Inhibitor Prodrugs

Nicholas P. Bigham[1], **Zhouyang Huang**[1,†], **Jesse Spivey**[1,†], **Joshua J. Woods**[1,2], **Samantha N. MacMillan**[1], **Justin J. Wilson**[1]

[1]Department of Chemistry and Biochemistry, Cornell University, Ithaca, NY, 14853, USA

[2]Robert F. Smith School of Engineering, Cornell University, Ithaca, NY, 14853, USA

Abstract

The mitochondrial calcium uniporter (MCU) is a transmembrane protein that resides on the inner membrane of the mitochondria and mediates calcium uptake into this organelle. Given the critical role of mitochondrial calcium trafficking in cellular function, inhibitors of this channel have arisen as tools for studying the biological relevance of this process and as potential therapeutic agents. In this study, four new analogues of the previously reported Ru-based MCU inhibitor $[ClRu(NH_3)_4(\mu\text{-}N)Ru(NH_3)_4Cl]Cl_3$ (Ru265) are reported. These compounds, which bear axial carboxylate ligands, are of the general formula $[(RCO_2)Ru(NH_3)_4(\mu\text{-}N)Ru(NH_3)_4(O_2CR)]X_3$, where X = NO_3^- or $CF_3SO_3^-$ and R = H (**1**), CH_3 (**2**), CH_2CH_3 (**3**), and $(CH_2)_2CH_3$ (**4**). These complexes were fully characterized by IR spectroscopy, NMR spectroscopy, and elemental analysis. X-ray crystal structures of **1** and **3** were obtained, revealing the expected presence of both the linear Ru(μ-N)Ru core and axial formate and propionate ligands. The axial carboxylate ligands of complexes **1**–**4** are displaced by water in buffered aqueous solution to give the aquated compound Ru265′. The kinetics of these processes were measured by ^{1}H NMR spectroscopy, revealing half-lives that span 5.9 to 9.9 h at 37 °C. Complex **1** with axial formate ligands underwent aquation approximately twice as fast as the other compounds. In vitro cytotoxicity

†Equal Contribution

Corresponding Author

Justin J. Wilson – Department of Chemistry and Chemical Biology, Cornell University, Ithaca, NY, 14853, United States; jjw275@cornell.edu

Authors

Nicholas P. Bigham – Department of Chemistry and Chemical Biology, Cornell University, Ithaca, NY, 14853, United States;

Zhouyang Huang – Department of Chemistry and Chemical Biology, Cornell University, Ithaca, NY, 14853, United States;

Jesse Spivey – Department of Chemistry and Chemical Biology, Cornell University, Ithaca, NY, 14853, United States

Joshua J. Woods – Department of Chemistry and Chemical Biology, Cornell University, Ithaca, NY 14853, United States; Robert F. Smith School for Chemical and Biomolecular Engineering, Cornell University, Ithaca, NY, 14853, United States;

Present Address: Chemical Sciences Division, Lawrence Berkeley National Laboratory, Berkeley, CA 94720, United States;

Samantha N. MacMillan – Department of Chemistry and Chemical Biology, Cornell University, Ithaca, NY, 14853, United States;

Associated Content

The Supporting Information is available free of charge at https://pubs.acs.org/doi/xxxxxxx

Complex characterization data including NMR and IR spectroscopy, and biological studies including cell viability curves, $_m Ca^{2+}$ uptake data, and cell stability studies (PDF)

Accession Codes

CCDC 2201612–2201613 contain the supplementary crystallographic data for this paper. These data can be obtained free of charge via www.ccdc.cam.ac.uk/data_request/cif, or by emailing data_request@ccdc.cam.ac.uk, or by contacting The Cambridge Crystallographic Data Centre, 12 Union Road, Cambridge CB2 1EZ, UK; fax: +44 1223 336033.

Conflict of Interest

The authors declare no conflict of interest.

and mitochondrial membrane potential measurements carried out in HeLa and HEK293T cells demonstrated that none of these four complexes negatively affects cell viability or mitochondrial function. The abilities of **1**–**4** to inhibit mitochondrial calcium uptake in permeabilized HEK293T cells were assessed and compared to that of Ru265. Fresh solutions of **1**–**4** are approximately 2-fold less potent than Ru265 with IC_{50} values in the range of 14.7 to 18.7 nM. Preincubating **1**–**4** in aqueous buffers for longer time periods to allow for the aquation reactions to proceed increases their potency of mitochondrial uptake inhibition to match that of Ru265. This result indicates that **1**–**4** are aquation-activated prodrugs of Ru265′. Lastly, **1**–**4** were shown to inhibit mitochondrial calcium uptake in intact, non-permeabilized cells, revealing their value as tools and potential therapeutic agents for mitochondrial calcium-related disorders.

Graphical Abstract

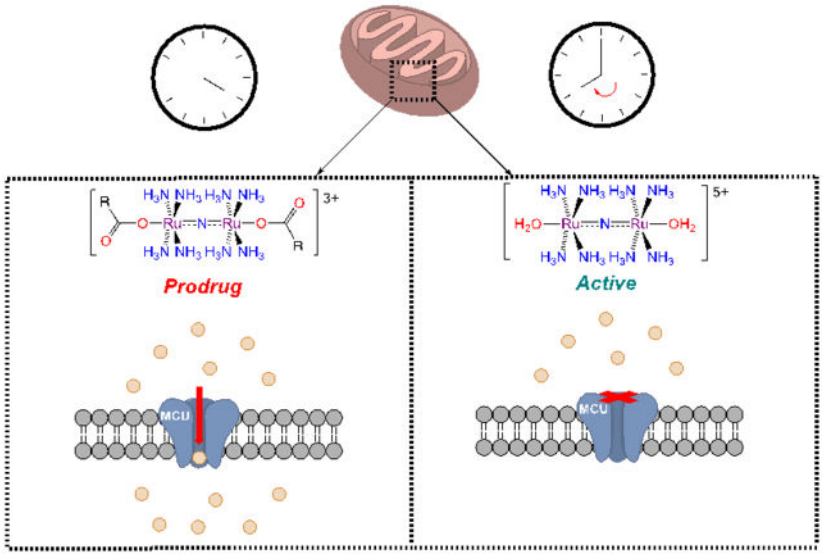

TOC Synopsis:

The mitochondrial calcium uniporter (MCU) is inhibited at nanomolar concentrations by the diruthenium complex known as Ru265. Modifying this complex at the axial site with carboxylate ligands results in complexes that are less potent MCU inhibitors. These carboxylate ligands exchange with water at physiological pH, releasing the diaqua analogue of Ru265. These complexes act as prodrugs for Ru265, suggesting a new way to develop and modify this class of MCU inhibitors.

Introduction

The homeostasis and dynamics of intracellular calcium ions (Ca^{2+}) are involved in a wide range of biological processes.[1–3] Among the key organelles responsible for Ca^{2+} regulation are the mitochondria. Mitochondrial Ca^{2+} ($_mCa^{2+}$) uptake is important for healthy cellular function, but dysregulation of this process can lead to deleterious effects. For example, $_mCa^{2+}$ overload triggers cell death[4,5] and has been implicated in a number of pathological conditions, including neurodegenerative disorders,[6,7] heart disease,[8–10] cancer,[11,12] cystic

fibrosis,[13,14] and ischemia-reperfusion injury.[15–17] Ca^{2+} influx into the mitochondria is mediated by the highly selective channel known as the mitochondrial calcium uniporter (MCU).[18–22] This transmembrane protein resides in the inner mitochondrial membrane (IMM) as a tetrameric assembly comprising the primary Ca^{2+}-transporting MCU subunit and the regulatory EMRE, MICU1, and MICU2 subunits.[23–32] Given the role of $_{m}Ca^{2+}$ overload within various diseases, inhibition of the MCU represents a promising therapeutic strategy.

To develop new therapeutic agents and tools for studying $_{m}Ca^{2+}$, extensive research efforts have been directed towards the identification of small-molecule MCU inhibitors.[33] To date, several organic[34–40] and inorganic[41–47] compounds have been discovered to possess MCU-inhibitory activity. Among these compounds, polynuclear Ru complexes are the oldest known MCU inhibitors, and recently developed analogues have shown promise for this application. The earliest inhibitor of this type identified is the trinuclear oxo-bridged complex ruthenium red (RuRed; Chart 1), which was originally applied as a cytological stain.[48] Subsequent studies, however, indicated that impurities present within RuRed samples were responsible for the $_{m}Ca^{2+}$ uptake-inhibitory activity.[41,49] These efforts ultimately led to the discovery of the dinuclear oxo-bridged complex Ru360 (Chart 1).[41,42,50] This complex exhibits nM potency as an MCU inhibitor in isolated mitochondria and permeabilized cells.[42,44] Its use in intact cell systems, however, has yielded inconsistent results — a possible consequence of its poor cell permeability and redox instability.[51]

Recently, an analogue of Ru360 called Ru265 was reported (Chart 1).[45] This compound is structurally similar to Ru360 but contains a bridging nitrido (N^{3-}) rather than an oxo (O^{2-}) ligand. In addition, the Ru centers in Ru265 are both in the +4 oxidation state, whereas Ru360 is a mixed valent Ru^{3+}/Ru^{4+} species. Notably, this relatively simple modification confers Ru265 with enhanced redox stability and the ability to inhibit $_{m}Ca^{2+}$ uptake in intact, non-permeabilized cells. These properties have been leveraged to elicit therapeutic effects in both in vitro and in vivo models of ischemic stroke.[52] The axial chloride ligands of Ru265 aquate on the order of minutes under physiological conditions, indicating that the active inhibitor is the diaqua-capped species Ru265′ (Chart 1). Accordingly, mutagenesis studies and molecular docking studies on the DIME region of the MCU, a highly conserved amino acid residue sequence that resides near the pore opening, revealed Ru265′ to bind at this site.[46]

Given that the axial chloride ligands of Ru265 rapidly dissociate and that the resulting Ru265′ is an active MCU inhibitor, we postulated that modifications to the axial sites of this compound class could afford an approach to develop prodrugs that possess improved properties for different biological applications (Scheme 1). Specifically, the implementation of less labile axial ligands would yield compounds whose pharmacokinetic, cellular uptake, and targeting properties could be optimized. In an initial effort towards these goals, we present in this study an investigation of alkyl carboxylates as suitable candidates for developing aquation-activated Ru265′ prodrugs. Four new derivatives of Ru265, bearing alkyl carboxylates of different carbon chain lengths as axial ligands, were synthesized and characterized (Chart 2). Encouragingly, the aquation kinetics of these complexes are substantially slower than those of Ru265, a property that can be leveraged for a time-

dependent increase in MCU-inhibitory activity. Through a series of cell biology studies, this work highlights the potential use of axial carboxylate ligands for the development of Ru265′ prodrugs through ligand dissociation.

Results and Discussion

Synthesis and Characterization

To explore the potential of oxygen donors as axial ligands for Ru265′ prodrugs, the smallest carbon chain carboxylates, formate, acetate, propionate, and butyrate, were investigated. The fact that Ru360 is isolated as the formate-capped species[41] and that recent 2D [^{1}H,^{15}N] heteronuclear single quantum coherence nuclear magnetic resonance (HSQC NMR) spectroscopic studies on ^{15}N-labeled Ru265 show this compound to covalently interact with aspartate and glutamate[53] demonstrates the viability of employing carboxylates as axial ligands for these dinuclear ruthenium complexes. Our choice of using these four carboxylates for these initial studies was motivated by the expected sequential enhancement in complex lipophilicity afforded by the systematic increase in carbon chain length. The calculated log *P* values for these carboxylic acids are −0.54, −0.28, 0.33, and 0.79 for formic, acetic, propanoic, and butyric acids, respectively, reflecting the magnitudes of increases in lipophilicity expected for the complexes. Cellular uptake is often correlated to lipophilicity,[54–61] and metal complexes bearing lipophilic groups have leveraged this property to enhance their therapeutic potentials.[62–67] We postulated that the use of these ligands could allow us to investigate this relationship for these Ru-based MCU inhibitors.

The general two-step syntheses required to access the formate (**1**), acetate (**2**), propionate (**3**), and butyrate (**4**) complexes are presented in Scheme 2. The reaction commenced from Ru265 by the addition of five equiv of either silver nitrate (**1**–**3**) or silver trifluoromethanesulfonate (triflate) (**4**) at 50 °C for 16 h in water to remove both the inner- and outer-sphere chlorides as insoluble silver chloride. The resulting aqueous solution of Ru265′ was then treated with two equiv of the sodium salt of the desired carboxylate to coordinate to the metal center in place of the coordinated water molecules and then allowed to heat at 50 °C for 16 h. This temperature and reaction time were chosen to maximize product yield, while preventing decomposition of the Ru(μ-N)Ru core, which can occur at higher temperatures. The nitrate salts of **1**–**3** were crystallized by the vapor diffusion of *p*-dioxane into an aqueous solution of the compounds containing 10% of their corresponding carboxylic acid to prevent aquation. For the triflate salt **4**, vapor diffusion of diethyl ether into a methanolic solution of the crude compound afforded analytically pure material.

The infrared (IR) spectra of **1**–**4** (Figures S1–4, SI) show diagnostic features that are consistent within their proposed structures. For **1**–**3**, an intense peak at 1383 cm^{-1}, which is the characteristic energy of the nitrate counterion stretching mode, is present. Within the IR spectrum of compound **4**, peaks diagnostic of the triflate counterion at 1269, 1223, 1145, and 637 cm^{-1} are observed.[68] The four complexes all give rise to intense peaks near 3400 cm^{-1}, 1600 cm^{-1}, and 1400 cm^{-1}, which arise from the N–H stretching modes of the ammine ligands and the symmetric and asymmetric C–O stretches of the carboxylates, respectively. Another key vibrational mode that is characteristic of these complexes is the asymmetric Ru–N–Ru stretch. For **2**–**4**, this mode is observed at 1039, 1040, and 1037 cm^{-1},

respectively. For **1**, this mode occurs at a slightly higher energy of 1064 cm^{-1}. The higher energy of the Ru–N–Ru stretch of **1** correlates with the lower basicity and weaker donor strength of the axial formate ligand compared to the alkyl carboxylates in **2**–**4**.

All four complexes give rise to well-resolved ^{1}H NMR spectra, consistent with their diamagnetic ground states (Figures S5–8, SI), that show characteristic resonances from both the equatorial ammine ligands and the axial carboxylates. The ^{1}H NMR resonance of the ammine ligands for all four complexes is apparent as a broad singlet near 3.95 ppm. For comparison, the chemical shift for the ammines of Ru265 resides further downfield at 4.15 ppm.[45] In the aqua-capped analogue Ru265′, however, the peak appears at 3.96 ppm (Figure S9, SI), like those observed for **1**–**4**. Thus, axial oxygen donors induce a small shielding effect on the protons of the ammine ligand, as has been shown previously.[53] Similarly, the ^{1}H resonances of the carboxylates are also shifted upfield by approximately 0.2 ppm relative to the free ligands. Further characterization by $^{13}C\{^{1}H\}$ (Figures S10–13, SI) and ^{19}F (Figure S14, SI) NMR spectroscopy of the complexes reveal the expected peaks for carboxylate ligands and the presence of the triflate counterion for **4**.

X-Ray Crystallography

Via the crystallization methods described above, single crystals of **3** suitable for X-ray diffraction were obtained. To grow X-ray diffraction-quality crystals of **1**, it was first converted to the triflate salt and then crystallized by the vapor diffusion of diethyl ether into a solution of it in methanol. The resulting crystal structures are shown in Figure 1, crystallographic data collection and refinement data are given in Table 1, and selected interatomic distances and angles are collected in Table 2. Notably, the asymmetric unit of **1** contains two molecules that are nearly identical. For simplicity, the structural data of just one of these molecules are tabulated in Table 2. Data for the second molecule in the asymmetric unit are presented in the SI (Table S1 **and** Figure S26, SI).

Both crystal structures reveal the linear Ru(μ-N)Ru core to remain intact with equatorial positions completed by the NH_3 ligands and the axial positions occupied by the corresponding carboxylates. The linearity of this motif is reflected by the Ru–N–Ru angles of 176.5(5) and 175.43(19)° for **1** and **3**, respectively. In addition, the Ru–N distances with the bridging nitrido range from 1.745(3) to 1.756(9) Å in **1** and **3**. These values are notably shorter than the Ru–N distances for the equatorial NH_3 ligands, which span 2.089(3) Å to 2.122(7) Å. The shorter Ru–N distance of the bridging nitrido is consistent with the multiple bonding character of this interaction. These values are similar to those of both Ru265 and Ru265′, for which the bridging Ru–N distances are 1.7421(7)[45] and 1.73871(15) Å[51], respectively. The axial Ru–O distances differ between **1** and **3**. For **3,** the Ru–O interatomic distances are 2.076(2) and 2.082(3) Å, whereas for **1**, they are on average slightly greater, ranging from 2.080(8) to 2.110(6) Å. Bond distance differences are considered significant if the difference is more than three times the standard uncertainty of their difference.[69] The average Ru–O bond distances of **1** are significantly different compared to the average Ru–O bond distances of **3**, given that their difference is four times the standard uncertainty of their differences. The longer distances within **1** may be a consequence of the weaker donor strength of formate compared to propionate, a property that is also reflected by the smaller

pK_a of formic acid. Notably, for both complexes these Ru–O distances are slightly shorter than those found in mononuclear Ru-carboxylate compounds, which typically fall within 2.00–2.200 Å.[70–74] These axial distances are longer, however, than the Ru–O interactions found within the crystal structure of the formate-capped Ru360, which is 2.033(3) Å.[41] The longer Ru–O axial distances found within **1** and **3** may be a consequence of the larger trans influence of the bridging nitrido present within these complexes compared to the bridging oxo ligand found in Ru360. The arrangement of the eight equatorial ammine ligands on each Ru center is staggered for **1** but eclipsed for **3**. Notably, within the structures of Ru265 and Ru265′ the ammine ligands are arranged in an eclipsed configuration. From an electronic and molecular orbital perspective, the eclipsed conformation is not required. This fact is reflected within the crystal structure of the ethylenediamine analogue of Ru265, which attains a staggered conformation.[45] Whether these complexes attain staggered versus eclipsed conformations is most likely a consequence of solid-state packing interactions. Lastly, intramolecular hydrogen-bonding interactions between the carboxylate and ammine ligands are present within both **1** and **3**. These interactions are similar to those frequently observed within carboxylate- or carbamate-bearing Pt^{4+} ammine complexes that have been used as prodrugs for cisplatin.[62,75]

Kinetics of Axial Carboxylate Dissociation via NMR Spectroscopy

With the carboxylate compounds **1**–**4** fully characterized, we sought to investigate their aquation kinetics. As previously noted, the axial chloride ligands of Ru265 are substituted by water within minutes under physiologically relevant conditions.[51] Thus, the viability of **1**–**4** as prodrugs for Ru265′ would require them exhibit substantially slower rates of aquation. To assess these properties, the complexes were incubated in pH 7.4 3-morpholinopropane-1-sulfonic acid (MOPS) buffered solution at 37 °C and monitored by ^{1}H NMR spectroscopy to follow the dissociation of the axial ligands over time. All complexes (**A**) underwent a sequential ligand substitution reaction with water to yield Ru265′ (**C**) via a detectable monoaquated intermediate **B**, as shown in Scheme 3.

As the aquation reactions progressed, resonances arising from the free ligand (**L**) and monoaquated species **B** arose, concomitant with the decay of the intact complex **A**, as shown in Figure 2a for **1** and Figures S15–17 **(**SI**)** for **2**–**4**. Their relative concentrations were determined by integrating the peaks of their ^{1}H NMR signals. Rate constants for both the first (k_1) and second (k_2) aquation steps were calculated by fitting the concentration vs time data to the established integrated rate laws for consecutive A → B → C kinetic process (Equations 1–4).[76] A representative data analysis for **1** is shown in Figure 2b. For **1**, the relative concentration of Ru265′ (**C**), which is not directly observable by ^{1}H NMR spectroscopy, was calculated using mass balance (Equation 5). For **2**–**4**, the ^{1}H NMR signals of **A** and **B**, overlap, thus requiring analysis using the sum of the concentrations of these species. The kinetics data for all four compounds are given in Table 3.

$$[A]_t = [A]_0 \exp(-k_1 t) \quad (1)$$

$$[B]_t = [B]_0 \exp\left(-k_2 t\right) + [A]_0 k_1 (k_2 - k_1)^{-1} \left\{\exp\left(-k_1 t\right) - \exp\left(-k_2 t\right)\right\} \quad (2)$$

$$[C]_t = [C]_0 + [B]_0\{1 - \exp(-k_2 t)\} + [A]_0(1 + \{k_1 \exp(-k_2 t) - k_2 \exp(-k_1 t)\}/(k_2 - k_1)) \quad (3)$$

$$[L]_t = [B]_t + 2[C]_t \quad (4)$$

$$[A]_t + [B]_t + [C]_t = 400\ \mu M \quad (5)$$

For all four complexes, k_1 was measured to be approximately an order of magnitude smaller than k_2. Thus, aquation of these carboxylate complexes is rate-limited by dissociation of the first ligand. This result is comparable to Ru265, for which aquation of the first chloride ligand is also an order of magnitude smaller than that of the second.[53] The half-lives of carboxylate ligand dissociation among the four complexes are on the order of hours. For comparison, the axial chloride ligands of Ru265 undergo aquation with a half-life of approximately 2 min under these same conditions.[51] Thus, the prolonged lifetime of the carboxylate-capped compounds portends to their potential use as prodrugs for Ru265′. In comparing the rate constants between compounds **1**–**4**, those of **1** are two to three times greater than those of **2**–**4**. The pK_a value of formic acid, the conjugate acid of the carboxylate ligand within **1**, is an order of magnitude smaller than the other alkyl carboxylates employed within **2**–**4**. Thus, the faster aquation rate of **1** correlates with the poorer basicity and donor strength of formate. Furthermore, as noted above in our discussion of the X-ray crystal structures, the interatomic axial Ru–O distances within **1** are longer than those found in **3**. Thus, ground state destabilization of **1** due to weaker Ru–O interactions appears to give rise to the faster dissociation rates observed within this complex. Collectively, these results demonstrate that axial position inertness of Ru265 analogues can be systematically tuned via the use of ligands of different donor strengths.

Cytotoxicity and Cellular Uptake

Key properties of Ru265 that make it valuable as an MCU inhibitor is its limited cytotoxicity and its ability to permeate the cell membrane, a feature that most likely arises from its high redox stability.[51] To assess the suitability of **1**–**4** in these contexts, we evaluated their cytotoxic effects and cellular uptake in both HeLa and HEK293T cells. The cytotoxicity of each complex was determined using the colorimetric thiazolyl blue tetrazolium bromide (MTT) assay. With 72 h incubation periods, the cell viability of both cell lines remained greater than 90% at concentrations up to 100 μM (Figures S18–S19, SI). In addition,

the JC-1 assay was used to verify that complexes **1**–**4** did not perturb the mitochondrial membrane potential of either cell line when administered at 50 μM for 24 h (Figures S20–22, SI). Having shown that **1**–**4** do not negatively affect cell viability or mitochondrial function, their cellular uptakes were next determined. Freshly thawed stock solutions of the four compounds as well as Ru265 were incubated at 50 μM for 2 h with both HeLa and HEK293T cells, and their intracellular accumulation was quantified by graphite furnace atomic absorption spectroscopy (GFAAS). As shown in Figure 3a, all four complexes and Ru265 are taken up by both cell lines to a similar extent. Thus, the presence of these different carboxylate ligands does not influence cellular uptake. This observation argues against a passive uptake mechanism for which increasing lipophilicity should correlate with enhanced cellular uptake.[54–56,58] We have previously reported that Ru265 enters cells through the organic cation transporter 3 (OCT3).[51] This transporter is upregulated in many tissues, including liver, heart, and skeletal muscle,[77,78] and facilitates the entry of organic cationic species like histamine, choline, dopamine, and norepinephrine.[79,80] To determine if **1**–**4** may similarly be substrates for the OCT3, their uptake in HeLa cells in the presence of the OCT3-specific inhibitor 1,1′-diethyl-2,2′-cyanine iodide (decynium-22) was determined. As shown in Figure 3b, only the uptake of Ru265 was diminished in the presence of the OCT3 inhibitor. These results suggest that OCT3 only mediates the uptake of Ru265 and not those of the carboxylate-capped analogues. Furthermore, these results also indicate that the carboxylate-capped species are entering cells in their intact forms, prior to aquation. After aquation, uptake of the resulting Ru265′ would be diminished in the presence of the OCT3 inhibitor.

Mitochondrial Ca^{2+} Uptake Inhibition in Permeabilized Cells

Given the favorable cellular uptake and lack of cytotoxicity of **1**–**4**, their MCU-inhibitory properties in digitonin-permeabilized HEK293T cells was investigated following established protocols.[81] In the presence of freshly prepared 1 μM solutions of either Ru265 or **1**–**4**, complete abrogation of $_{m}Ca^{2+}$ uptake was observed in these permeabilized cells. The administered concentrations for each compound were varied to obtain dose-response curves for MCU inhibition from which 50% inhibitory concentration (IC_{50}) values were determined (Figures S23 and S24, SI). All four complexes exhibit nanomolar potency but are approximately two-fold less active than Ru265 (Table 4).

Although **1**–**4** are slightly less potent than Ru265, their ability to aquate within the hour timescale to yield Ru265′ prompted us to investigate their time-dependent MCU-inhibitory properties. Before assessing MCU inhibition in permeabilized HEK293T cells, each complex was incubated in pH 7.4 MOPS-buffered solution for 1, 3, or 6 h at 37 °C. After these incubation periods, the aged solutions were diluted to 10 nM, and their $_{m}Ca^{2+}$ uptake-inhibitory properties were determined. The transient curves of these experiments, showing the fluorescence response of the Calcium Green 5N sensor, demonstrate that $_{m}Ca^{2+}$ uptake is increasingly impaired for complexes that were preincubated for longer time periods. (Figure S25, SI). The normalized $_{m}Ca^{2+}$ uptake rates plotted as a function of buffer preincubation time periods are shown in Figure 4. These data reveal all four carboxylate complexes to attain the same MCU-inhibitory activity as Ru265′ after an incubation period

of 6 h. These results suggest that axial ligand modification of Ru265 provides an effective means of generating aquation-activated prodrugs for Ru265′.

Intact Cell Mitochondrial Ca^{2+} Uptake Inhibition

Having demonstrated that **1**–**4** are active MCU inhibitors in permeabilized cells, we next sought to determine their ability to operate in intact cell systems like Ru265.[45] The mitochondria-localizing dye Rhod-2-AM was incubated with HeLa cells that were treated with 50 μM of each complex for 1 h at 37 °C. Histamine was added to the cells to stimulate mitochondrial Ca^{2+} uptake, and the fluorescence response was measured and compared to nontreated cells. As was expected, Ru265 and the derivatives discussed in this work showed a decreased fluorescence response in comparison to untreated cells, as shown in Figure 5. These results demonstrate that these compounds maintain their potent MCU-inhibitory activity in intact cell systems.

Conclusions

In this work, four analogues of the potent MCU inhibitor Ru265 were described. These analogues, which contain axial carboxylate ligands, undergo aquation on the timescale of hours at 37 °C, releasing the diaqua-capped complex Ru265′. Importantly, we demonstrated that the intact carboxylate-capped species are less effective MCU inhibitors than Ru265′, but upon aquation and formation of Ru265′ they are equally potent. This result highlights that axial ligand modification represents a viable approach to develop prodrugs for Ru265′. The success of this strategy is important because we have previously shown that alteration of the equatorial ligands on the Ru(μ-N)Ru core yields compounds that have significantly diminished or non-existent MCU-inhibitory properties.[45,51,82] Therefore, it appears that changes to the axial ligand represent the best strategy for fine-tuning the biological properties of this compound class without sacrificing the uptake and inhibitory efficacy. In addition, a comparison of the formate-capped complex **1** and the other alkyl carboxylate-capped complexes revealed the former to undergo aquation faster. Thus, the choice of appropriate axial ligands can have important impacts on the rate of prodrug activation, providing another means for modifying and optimizing compounds within this class for different biological applications. We envision that these studies will lay the groundwork for designing Ru265 analogues containing functional axial ligands with targeting capabilities or secondary biological activities. These types of modifications will allow for new more effective tools to study $_{m}Ca^{2+}$ dynamics and potential therapeutic agents for the treatment of conditions that are mediated by $_{m}Ca^{2+}$ dysregulation.

Experimental Section

Reagents and Materials

All reagents were obtained commercially and used without further purification. Ru265 was prepared as previously described.[45] Water (18 MΩ·cm) was purified using an ELGA PURELAB flex 2 (High Wycombe, UK).

Physical Measurements

1D-NMR (^{1}H, ^{13}C{^{1}H}, and ^{19}F) spectra were acquired at 25 °C on a 500 MHz Bruker AV 3HD spectrometer equipped with a broadband Prodigy cryoprobe (Bruker, Billerica, MA). Elemental analyses (C, H, N) were carried out by Atlantic Microlab Inc. (Norcross, GA). Fluorescence and absorbance of samples in 96-well plates were measured using a BioTek Synergy HT plate reader (Winooski, VT). GFAAS was performed using a PinAAcle 900Z spectrometer (Perkin Elmer, Waltham, MA). Standardized solutions (0–200 μg/L) of ruthenium were used to generate a calibration curve. The concentrations of all ruthenium stock solutions applied in analytical and biological experiments were verified by GFAAS. Statistical analyses were performed using GraphPad Prism version 9.4.1 by applying a non-paired student's t-test. Curve fitting was also performed using GraphPad Prism version 9.4.1 for Mac OS, GraphPad Software, San Diego, California USA.

Cell Lines and Culture Conditions

HeLa and HEK293T cells were obtained from American Type Culture Collection (ATCC, Washington DC) and cultured at 37 °C as adherent monolayers in a humidified atmosphere containing 5% CO_2 in Dulbecco's Modified Eagle's Medium (DMEM) containing 4.5 g/L glucose, L-glutamine, and 3.7 g/L sodium bicarbonate supplemented with 10% fetal bovine serum (FBS). Cells were tested for mycoplasma contamination bimonthly through the commercial service provided by the College of Veterinary Medicine at Cornell University. All reagents and solutions used in biological studies were sterile filtered through a 0.2 μm filter and maintained under sterile conditions.

Synthesis of $[(HCO_2)Ru(NH_3)_4(\mu\text{-}N)Ru(NH_3)_4(O_2CH)](NO_3)_3$ (1)

Ru265 (100 mg, 0.189 mmol) was dissolved in 15 mL 18 MΩ·cm H_2O, and solid $AgNO_3$ (160 mg, 0.950 mmol; Alfa Aesar) was added to this solution. The reaction mixture was stirred at 50 °C in the dark for 12 h. The resulting cloudy, orange suspension was filtered through celite to remove the precipitated AgCl. The orange filtrate was then treated with solid sodium formate (26 mg, 0.378 mmol; Fluka Chemical Corporation) and stirred at 50 °C for 12 h. After cooling to room temperature, the orange solution was concentrated to dryness under vacuum, leaving an orange solid. This solid was dissolved in 1 mL 10% formic acid in water. Orange crystals of the desired compound were obtained by the vapor diffusion of *p*-dioxane into this solution over the course of 3 d at room temperature. The mother liquor was decanted, and the remaining orange crystals were washed sequentially with 15 mL ethanol, 15 mL methanol, and 15 mL acetone, before drying under vacuum. Yield: 29.7 mg (0.047 mmol, 25%). ^{1}H NMR (500 MHz, DMSO-d_6) δ (ppm) = 4.01 (s, 24H), 8.12 (s, 2H). ^{13}C{^{1}H} NMR (126 MHz, DMSO-d_6) δ (ppm) = 170.02. IR (ATR) ν (cm^{-1}) = 3295 (s, br), 1606 (m), 1384 (s), 1063 (m), 830 (m). Elemental analysis: calc'd (%, for $C_2H_{26}N_{12}O_{13}Ru_2 \cdot 3.5H_2O$) C 3.47; H 4.81; N 24.31. Found (%) C 3.74; H 4.72; N 24.11.

Synthesis of $[(CH_3CO_2)Ru(NH_3)_4(\mu\text{-}N)Ru(NH_3)_4(O_2CCH_3)](NO_3)_3$ (2)

The synthesis of **2** was carried out following the procedure described for **1**, using the same quantities of Ru265 and $AgNO_3$. In place of sodium formate, sodium acetate (31 mg, 0.378 mmol; Fluka Chemical Corporation) was used, and the crystallization employed 10% acetic

acid instead of 10% formic acid. Yield: 26.0 mg (0.040 mmol, 21%). ^{1}H NMR (500 MHz, DMSO-d_6) δ (ppm) = 3.95 (s, 24H), 1.77 (s, 6H). ^{13}C{^{1}H} NMR (126 MHz, DMSO-d_6) δ (ppm) = 178.83, 24.94. IR (ATR) ν (cm^{-1}) = 3295 (s, br), 1575 (m), 1384 (s), 1040 (m), 830 (m). Elemental analysis: calc'd (%, for $C_4H_{30}N_{12}O_{13}Ru_2 \cdot H_2O$) C 7.12; H 4.78; N 24.92. Found (%) C 7.09; H 4.65; N 24.71.

Synthesis of $[(CH_3CH_2CO_2)Ru(NH_3)_4(\mu\text{-}N)Ru(NH_3)_4(O_2CCH_2CH_3)](NO_3)_3$ (3)

The synthesis of **3** was carried out following the procedure described for **1**, using the same quantities of Ru265 and $AgNO_3$. In place of sodium formate, sodium propionate (36 mg, 0.378 mmol; Alfa Aesar) was used, and the crystallization employed 10% propanoic acid instead of 10% formic acid. Yield: 18.1 mg (0.026 mmol, 14%). ^{1}H NMR (500 MHz, DMSO-d_6) δ (ppm) = 3.96 (s, 24H), 2.05 (q, 4H, J = 7.5 Hz), 0.92 (t, 6H, J = 7.5 Hz). ^{13}C{^{1}H} NMR (126 MHz, DMSO-d_6) δ (ppm) = 181.76, 30.33, 10.05. IR (ATR) ν (cm^{-1}) = 3295 (s, br), 1565 (m), 1384 (s), 1048 (m), 830 (m). Elemental analysis: calc'd (%, for $C_6H_{34}N_{12}O_{13}Ru_2 \cdot 1.5H_2O$) C 10.13; H 5.24; N 23.62. Found (%) C 10.09; H 4.81; N 23.72.

Synthesis of $[(CH_3(CH_2)_2CO_2)Ru(NH_3)_4(\mu\text{-}N)Ru(NH_3)_4(O_2C(CH_2)_2CH_3)](OSO_2CF_3)_3$ (4)

Ru265 (100 mg, 0.189 mmol) was dissolved in 15 mL 18 MΩ·cm H_2O. Solid $AgOSO_2CF_3$ (243 mg, 0.950 mmol; Aldrich Chemical Company) was added, and the reaction mixture was stirred at reflux for 3 h in the dark. Insoluble AgCl was removed by filtration through celite, and sodium butyrate (41 mg, 0.378 mmol; Aldrich Chemical Company) was added to the orange filtrate, which was then stirred at 50 °C for 12 h. The orange solution was cooled to room temperature and concentrated to dryness under vacuum to yield an orange solid. This solid was dissolved in 1 mL of methanol and crystallized by allowing diethyl ether to vapor diffuse into this solution at room temperature over the course of 2 d. The resulting orange crystals were washed sequentially with 15 mL acetone and 15 mL diethyl ether, and then dried under vacuum. Yield: 14.7 mg (0.015 mmol, 8%). ^{1}H NMR (500 MHz, DMSO-d_6) δ (ppm) = 3.92 (s, 24H), 2.01 (t, 4H, J = 7.5 Hz), 1.45 (q, 4H, J = 7.5 Hz), 0.83 (t, 6H, J = 7.5 Hz). ^{13}C{^{1}H} NMR (126 MHz, DMSO-d_6) δ (ppm) = 181.80, 31.17, 19.22, 14.52. ^{19}F NMR (470 MHz, DMSO-d_6) δ (ppm) = −77.75. IR (ATR) ν (cm^{-1}) = 3295 (m, br), 1603 (m), 1253 (s), 1170 (s), 1033 (m), 830 (w), 632 (m), 516 (w). Elemental analysis: calc'd (%, for $C_{11}H_{38}N_9O_{13}F_9S_3Ru_2 \cdot CH_3OH$) C 14.33; H 4.21; N 12.53. Found (%) C 14.09; H 4.28; N 12.30.

X-Ray Crystallography

Single crystals of **3** were obtained via the vapor diffusion of *p*-dioxane into aqueous solutions of the compound in 10% propionic acid at room temperature. Compound **1** was converted to the triflate salt, and single crystals were obtained via the vapor diffusion of diethyl ether into a methanolic solution this compound at room temperature. Low-temperature X-ray diffraction data for **1** and **3** were collected on a Rigaku XtaLAB Synergy diffractometer coupled to a Rigaku Hypix detector with either Mo Kα radiation (λ = 0.71073 Å) or Cu Kα radiation (λ = 1.54184 Å), from PhotonJet micro-focus X-ray sources at 100 K. The diffraction images were processed and scaled using the CrysAlisPro software (Rigaku Oxford Diffraction, The Woodlands TX). The structures were solved

through intrinsic phasing using SHELXT[83] and refined against F^2 on all data by full matrix least squares with SHELXL[84] following established refinement strategies.[85] All non-hydrogen atoms were refined anisotropically. All hydrogen atoms bound to carbon were included in the model at geometrically calculated positions and refined using a riding model. Hydrogen atoms bound to oxygen were located in the difference Fourier synthesis and subsequently refined semi-freely with the help of distance restraints. The isotropic displacement parameters of all hydrogen atoms were fixed to 1.2 times the Ueq value of the atoms they are linked to (1.5 times for methyl groups). Compound **1** crystallized in the space group $P2_1/c$; the crystal is twinned and the structure was refined using an HKLF 5 file containing data for two twin domains, with a refined BASF of 0.1824(8). Details of the data quality and a summary of the residual values of the refinements are listed in Tables 1–2 and S1. The B-level alert that arose in the checkCIF file can be explained by hydrogen bonding of the methanol solvent molecule to the nitrogen groups of the complex **1**. The short interatomic distance between this solvent oxygen and the oxygen of the formate ligand is thus due to the hydrogen bonding of the solvent to the complex.

Compound **1** crystallized in the space group $P2_1/c$; the crystal is twinned and the structure was refined using an HKLF 5 file containing data for two twin domains, with a refined BASF of 0.1965(9). Within the asymmetric unit, two molecules of the complex cation were present, along with six triflate counterions and three methanol molecules. Two of the three methanol molecules were disordered about two distinct orientations and refined accordingly with appropriate similarity restraints, constraining the sum of the occupancy to be 1. Likewise, rotational and positional disorder was identified in three of the triflate counterions and was refined accordingly. Lastly, one of the coordinated formate ligands was modeled as being disordered about two orientations. CheckCIF analysis of the structure of **1** reveals a B-level alert that arises from a short contact (2.70 Å) between atoms O1S and O8. O1S belongs to a methanol molecule present within the crystal lattice and O8 belongs to the non-coordinating formate ligand of one of the complex cations. This close-contact is a consequence of a likely hydrogen-bonding interaction between these two molecules. The alert is triggered by the fact that the hydrogen atom of the methanol was not included in the refinement model, because it could not be definitively located on the difference Fourier map.

NMR Kinetics Studies

Aqueous solutions were prepared to contain 400 μM complex, 40 mM MOPS buffer (pH 7.4), 10% D_2O for NMR field-locking, and 0.1% *p*-dioxane as an internal reference (δ = 3.75 ppm in D_2O). The aquation of complexes at 37 °C was monitored via the evolution of selected proton resonances arising from the carboxylate functional groups in the ^1H NMR spectra. The concentrations of the starting materials (**A**), mono-aquated intermediates (**B**), and free ligands (**L**) were calculated using the relative integration of the corresponding proton resonances. Rate constants were calculated by fitting the concentration vs time data to the established integrated rate laws for consecutive reactions (Equations 1–5) using GraphPad Prism.

Cytotoxicity Assay

HeLa and HEK293T cells were seeded in 96-well plates with ~4000 cells/well and incubated overnight. On the following day, the culture media was removed, and cells were treated with media containing varying concentrations of the test complex and incubated for 72 h. The cells were then incubated in DMEM containing 1 mg/mL MTT without FBS for 3 h. Following incubation, the media was removed, and the purple formazan crystals were dissolved in 200 μL of an 8:1 DMSO/glycine buffer (pH 10) mixture. The absorbance at 570 nm of each well was measured using a BioTek Synergy HT plate reader. The average absorbance of control cells was set to 100% viability, and the average absorbances of treated cells were normalized to the control absorbance. Data were plotted as percent viability versus the log[concentration]. The Hill Equation was applied to the data to determine the IC_{50}. Data are reported as the average of three independent biological replicates ± SD.

Mitochondrial Membrane Potential via JC-1 Assay

Approximately 1×10^5 HeLa or HEK293T cells were seeded in 35 mm glass-bottomed dishes (MatTek Life Sciences, Ashland, MA) and incubated overnight at 37 °C. On the next day, cells were treated with the desired complex (50 μM) and incubated for an additional 24 h at 37 °C. The culture media was then removed and replaced with fresh media supplemented with 10 μM JC-1 dye, followed by incubation in the dark for 30 min at 37 °C. The dye-containing media was removed, and the cells were washed with 2 × 1 mL phosphate-buffered saline (PBS, Corning Life Sciences). The cells were imaged in 1 mL PBS. Control dishes were handled identically to treated dishes. For the positive control dishes, 50 μM carbonyl cyanide *m*-chlorophenyl hydrazine (CCCP) in PBS was used, and the images were collected without the removal of CCCP. The cells were imaged using an EVOS M5000 fluorescence microscope (ThermoFisher, Waltham, MA) with a green fluorescence protein (GFP) filter cube (ex. 457–487/em. 502–538) for the green monomer fluorescence and a Texas red filter cube (ex. 542–582/em. 604–644) for the red J-aggregate fluorescence. The cellular images were analyzed using ImageJ (NIH) and the corrected total cellular fluorescence (CTCF) was calculated using the following formula:

$$\mathrm{CTCF} = \mathrm{Integrated} - (\mathrm{area\ of\ cell} \times \mathrm{mean\ fluorescence\ of\ background\ reading})$$

For each replicate, the average red/green fluorescence was determined using at least 8 independent cells and was normalized to untreated control cells ($[\mathrm{red/green}]_{\mathrm{control}} = 1$). Data are reported as the average of three independent trials ± SD.

Cell Uptake

HeLa and HEK293T cells were grown to near confluence in 6-well plates. On the day of the experiment, the culture media was removed, and the cells were treated with fresh media containing 0 or 50 μM complex and incubated for 2 h at 37 °C. The culture media was then removed, and the adherent cells were washed with PBS, detached with 0.05% trypsin + 0.53 mM ethylenediaminetetraacetic acid (EDTA; Corning Life Sciences), and then pelleted by centrifugation (800 × *g* for 10 min). The cell pellet was suspended in ice cold lysis buffer (1% w/v 3-[3-cholamidopropyl)dimethylammonio]-1-propanesulfonate (CHAPS), 5

mM EDTA, 50 mM tris(hydroxymethyl)aminomethane (Tris) and 100 mM NaCl; pH 7.4). The suspension was vortexed for 30 s and incubated on ice for 45 min. The cell lysate was centrifuged to remove precipitated debris and the supernatant was transferred to a clean tube prior to analysis. The Ru content of the lysate was determined using GFAAS and was normalized to the protein content of the sample, which was determined using the bicinchoninic acid (BCA) assay kit following manufacturer instructions (ThermoFisher). Results are reported as the average mass ratio of Ru to protein (pg/μg) in each sample ± SD.

Role of OCT3 in Cellular Uptake

Approximately 1×10^5 HeLa cells were seeded in 6-well plates and incubated at 37 °C overnight. On the next day, the culture media was removed, and the cells were treated with fresh media supplemented with the test complex (50 μM) and the OCT3 inhibitor decynium-22 (1 μM). The cells were incubated for 3 h before they were washed, harvested, lysed, and analyzed as described above. Results are reported as the average mass ratio of Ru to protein (pg/μg) in each sample ± SD.

Mitochondrial Ca^{2+} Uptake in Permeabilized HEK293T Cells

HEK293T cells were grown to near confluency in a 10 cm^2 dish and harvested with trypsin. The cells were pelleted by centrifugation, suspended in cold PBS supplemented with 5 mM EDTA (pH 7.4), and counted using trypan blue. The cells were pelleted by centrifugation at 800 × *g* for 5 min and resuspended in ice cold KCl solution (125 mM KCl, 20 mM 4-(2-hydroxyethyl)-1-piperazineethanesulfonic acid (HEPES), 2 mM K_2HPO_4, 5 mM glutamate, 5 mM malate, 1 mM $MgCl_2$, pH 7.2 with KOH) supplemented with 80 μM digitonin and 1 μM thapsigargin. The final solution contained <0.1% DMSO, originating from the digitonin and thapsigargin stocks. The cells were incubated on ice for 15 min and centrifuged at 200 × *g* for 10 minutes at 4°C. The pelleted cells were then resuspended in high KCl solution containing 1 μM Calcium Green 5N (ThermoFisher, Waltham, MA) and 2 mM succinate to a final density of 1×10^7 cells/mL. For each experiment, 100 μL of the cell suspension was placed in each well of a black-walled 96-well plate, treated with the desired concentration of the test complex, and allowed to equilibrate at room temperature for ~200 s. The background fluorescence of each well was recorded for 60 s prior to addition of 20 μM $CaCl_2$. The change in fluorescence of the dye (ex. 488/em. 528) in response to Ca^{2+} was recorded every 5 s for at least 120 s or until the fluorescence returned to the baseline. The $_mCa^{2+}$ uptake rate was calculated as the time constant in the exponential fit of the decay in fluorescence response curve. Control cells that were not treated with compound were handled identically to the treated cells to account for different incubation lengths. The Ca^{2+} uptake rate of treated cells was normalized to that of the control cells (0% inhibition), and each replicate was performed using independently prepared cell suspensions to account for differences in cell count. A BCA assay was performed on each cell suspension for every experiment, giving a protein content of ~1200 μg mL^{-1} each time. The Hill Equation was used to determine the IC_{50} of MCU inhibition. Data are presented as the average of three independent biological replicates ± SD.

Time-Dependent Mitochondrial Ca^{2+} Uptake Experiments

Aqueous solutions of 400 μM complex were prepared in 40 mM MOPS buffer (pH 7.4; 100-fold excess buffer). The solutions were incubated at 37 °C for 1, 3, and 6 h before being immediately frozen in liquid nitrogen. Each solution was stored at −80 °C until the $_{m}Ca^{2+}$ uptake experiments were performed. Each stock solution was then diluted in 18 MΩ·cm H_2O to a final concentration of 10 nM complex in the black-walled 96-well plates (200 nM complex before dilution with cell suspension). The $_{m}Ca^{2+}$ uptake assay was performed as described above with a concentration of 1×10^7 HEK293T cells/mL. Data were analyzed as described above and presented as the average $_{m}Ca^{2+}$ uptake rate of three independent biological replicates ± SD.

Mitochondrial Ca^{2+} Uptake in Intact HeLa Cells using Rhod2AM

Approximately 5×10^4 HeLa cells were seeded in an 8-well μ-slide (Ibidi USA, Inc., Fitchburg, WI) and incubated overnight at 37 °C. The following day, cells were treated with the desired metal complex (50 μM) in DMEM supplemented with 10% FBS for 1 h at 37 °C. The culture media was removed, and the cells were washed with 1 × 1 mL PBS before the cells were incubated in extracellular medium (ECM; 135 mM NaCl, 20 mM HEPES, 5 mM KCl, 1 mM $MgCl_2$, 1 mM $CaCl_2$) supplemented with 10 mM glucose, 3.2 mg mL^{-1} bovine serum albumin (BSA), 0.003% Pluronic F127, and 2 μM Rhod2AM (Molecular Probes) in the dark for 30 min at room temperature. The ECM was then removed, the cells were washed with 1 × 1 mL ECM, and the cells were treated with fresh ECM supplemented with 10 mM glucose and 3.2 mg/mL BSA and incubated for an additional 30 min in the dark at room temperature. The buffer was then removed and the cells washed with 1 × 1 mL ECM and treated with ECM supplemented with 10 mM glucose and 3.2 mg/mL BSA. The cells were incubated for 15 min at 37 °C before imaging using a Zeiss LSM i710 confocal microscope using a 40× oil objective with an excitation of 561 nm and an emission window of 568–712 nm. After ~ 30 s of baseline recording, histamine (final concentration of 100 μM) was added to the dish and fluorescence images were collected every 3 s to monitor $_{m}Ca^{2+}$ uptake. Images were analyzed and quantified using ImageJ and the CTCF was calculated. The average of at least six individual cells were used to determine the average CTCF for each replicate. Results are reported as the average of two independent replicates ± SD.

Supplementary Material

Refer to Web version on PubMed Central for supplementary material.

Acknowledgments

This research was supported by Cornell University, the United States National Science Foundation (NSF) under award number CHE-1750295, the Research Corporation for Science Advancement through a Cottrell Scholar Award, and the American Heart Association (AHA Predoctoral Fellowship to J. J. Woods; award no. 20PRE35120390). This work made use of the Cornell University NMR facility, which is supported by the NSF under award number CHE-1531632. Additional resources included the use of the Cornell University Biotechnology Resource Center, which is supported by the NIH (NIH S10RR025502).

References

(1). Pozzan T; Rizzuto R; Volpe P; Meldolesi J Molecular and Cellular Physiology of Intracellular Calcium Stores. Physiol. Rev 1994, 74, 595–636. [PubMed: 8036248]

(2). Berridge MJ; Bootman MD; Roderick HL Calcium Signalling: Dynamics, Homeostasis and Remodelling. Nat. Rev. Mol. Cell Biol 2003, 4, 517–529. [PubMed: 12838335]

(3). Clapham DE Calcium Signaling. Cell 2007, 131, 1047–1058. [PubMed: 18083096]

(4). Carafoli E; Brini M Calcium Signalling and Disease: Molecular Pathology of Calcium. In Subcellular Biochemistry; Springer: New York, NY, 2007; Vol. 45, pp 481–506. [PubMed: 18193649]

(5). Orrenius S; Gogvadze V; Zhivotovsky B Calcium and Mitochondria in the Regulation of Cell Death. Biochem. Biophys. Res. Commun 2015, 460, 72–81. [PubMed: 25998735]

(6). Celsi F; Pizzo P; Brini M; Leo S; Fotino C; Pinton P; Rizzuto R Mitochondria, Calcium and Cell Death: A Deadly Triad in Neurodegeneration. Biochim. Biophys. Acta - Bioenerg 2009, 1787, 335–344.

(7). Abeti R; Abramov AY Mitochondrial Ca^{2+} in Neurodegenerative Disorders. Pharmacol. Res 2015, 99, 377–381. [PubMed: 26013908]

(8). Gustafsson ÅB; Gottlieb RA Heart Mitochondria: Gates of Life and Death. Cardiovasc. Res 2008, 77, 334–343. [PubMed: 18006487]

(9). Santulli G; Xie W; Reiken SR; Marks AR Mitochondrial Calcium Overload Is a Key Determinant in Heart Failure. Proc. Natl. Acad. Sci. U. S. A 2015, 112, 11389–11394. [PubMed: 26217001]

(10). Zhou B; Tian R Mitochondrial Dysfunction in Pathophysiology of Heart Failure. J. Clin. Invest 2018, 128, 3716–3726. [PubMed: 30124471]

(11). Vultur A; Gibhardt CS; Stanisz H; Bogeski I The Role of the Mitochondrial Calcium Uniporter (MCU) Complex in Cancer. Pflugers Arch. Eur. J. Physiol 2018, 470, 1149–1163. [PubMed: 29926229]

(12). Delierneux C; Kouba S; Shanmughapriya S; Potier-Cartereau M; Trebak M; Hempel N Mitochondrial Calcium Regulation of Redox Signaling in Cancer. Cells 2020, 9, 432. [PubMed: 32059571]

(13). Rimessi A; Pozzato C; Carparelli L; Rossi A; Ranucci S; de Fino I; Cigana C; Talarico A; Wieckowski MR; Ribeiro CMP; Trapella C; Rossi G; Cabrini G; Bragonzi A; Pinton P Pharmacological Modulation of Mitochondrial Calcium Uniporter Controls Lung Inflammation in Cystic Fibrosis. Sci. Adv 2020, 6, eaax9093. [PubMed: 32494695]

(14). Rimessi A; Vitto VAM; Patergnani S; Pinton P Update on Calcium Signaling in Cystic Fibrosis Lung Disease. Front. Pharmacol 2021, 12, 581645. [PubMed: 33776759]

(15). Halestrap AP Calcium, Mitochondria and Reperfusion Injury: A Pore Way to Die. Biochem. Soc. Trans 2006, 34, 232–237. [PubMed: 16545083]

(16). Shintani-Ishida K; Inui M; Yoshida K Ischemia-Reperfusion Induces Myocardial Infarction through Mitochondrial Ca^{2+} Overload. J. Mol. Cell. Cardiol 2012, 53, 233–239. [PubMed: 22659291]

(17). Sanderson TH; Reynolds CA; Kumar R; Przyklenk K; Huttemann M Molecular Mechanisms of Ischemia-Reperfusion Injury in Brain: Pivotal Role of the Mitochondrial Membrane Potential in Reactive Oxygen Species Generation. Mol. Neuorobiol 2013, 47, 9–23.

(18). Kirichok Y; Krapivinsky G; Clapham DE The Mitochondrial Calcium Uniporter Is a Highly Selective Ion Channel. Nature 2004, 427, 360–364. [PubMed: 14737170]

(19). Baughman JM; Perocchi F; Girgis HS; Plovanich M; Belcher-Timme CA; Sancak Y; Bao XR; Strittmatter L; Goldberger O; Bogorad RL; Koteliansky V; Mootha VK Integrative Genomics Identifies MCU as an Essential Component of the Mitochondrial Calcium Uniporter. Nature 2011, 476, 341–345. [PubMed: 21685886]

(20). Rizzuto R; De Stefani D; Raffaello A; Mammucari C Mitochondria as Sensors and Regulators of Calcium Signalling. Nat. Rev. Mol. Cell Biol 2012, 13, 566–578. [PubMed: 22850819]

(21). Kamer KJ; Mootha VK The Molecular Era of the Mitochondrial Calcium Uniporter. Nat. Rev. Mol. Cell Biol 2015, 16, 545–553. [PubMed: 26285678]

(22). Nemani N; Shanmughapriya S; Madesh M Molecular Regulation of MCU: Implications in Physiology and Disease. Cell Calcium 2018, 74, 86–93. [PubMed: 29980025]

(23). De Stefani D; Raffaello A; Teardo E; Szabó I; Rizzuto R A Forty-Kilodalton Protein of the Inner Membrane Is the Mitochondrial Calcium Uniporter. Nature 2011, 476, 336–340. [PubMed: 21685888]

(24). Oxenoid K; Dong Y; Cao C; Cui T; Sancak Y; Markhard AL; Grabarek Z; Kong L; Liu Z; Ouyang B; Cong Y; Mootha VK; Chou JJ Architecture of the Mitochondrial Calcium Uniporter. Nature 2016, 533, 269–273. [PubMed: 27135929]

(25). Fan C; Fan M; Orlando BJ; Fastman NM; Zhang J; Xu Y; Chambers MG; Xu X; Perry K; Liao M; Feng L X-Ray and Cryo-EM Structures of the Mitochondrial Calcium Uniporter. Nature 2018, 559, 575–579. [PubMed: 29995856]

(26). Baradaran R; Wang C; Siliciano AF; Long SB Cryo-EM Structures of Fungal and Metazoan Mitochondrial Calcium Uniporters. Nature 2018, 559, 580–584. [PubMed: 29995857]

(27). Nguyen NX; Armache J-P; Lee C; Yang Y; Zeng W; Mootha VK; Cheng Y; Bai X-C; Jiang Y Cryo-EM Structure of a Fungal Mitochondrial Calcium Uniporter. Nature 2018, 559, 570–574. [PubMed: 29995855]

(28). Fan M; Zhang J; Tsai C-W; Orlando BJ; Rodriguez M; Xu Y; Liao M; Tsai M-F; Feng L Structure and Mechanism of the Mitochondrial Ca2+ Uniporter Holocomplex. Nature 2020, 582, 129–133. [PubMed: 32494073]

(29). Wang Y; Nguyen NX; She J; Zeng W; Yang Y; Bai X-C; Jiang Y Structural Mechanism of EMRE-Dependent Gating of the Human Mitochondrial Calcium Uniporter. Cell 2019, 177, 1252–1261. [PubMed: 31080062]

(30). Vais H; Payne R; Paudel U; Li C; Foskett JK Coupled Transmembrane Mechanisms Control MCU-Mediated Mitochondrial Ca^{2+} Uptake. Proc. Natl. Acad. Sci. U. S. A 2020, 117, 21731–21739. [PubMed: 32801213]

(31). Wang C; Baradaran R; Long SB Structure and Reconstitution of an MCU–EMRE Mitochondrial Ca^{2+} Uniporter Complex. J. Mol. Biol 2020, 432, 5632–5648. [PubMed: 32841658]

(32). Zhuo W; Zhou H; Guo R; Yi J; Zhang L; Yu L; Sui Y; Zeng W; Wang P; Yang M Structure of Intact Human MCU Supercomplex with the Auxiliary MICU Subunits. Protein Cell 2021, 12, 220–229. [PubMed: 32862359]

(33). Woods JJ; Wilson JJ Inhibitors of the Mitochondrial Calcium Uniporter for the Treatment of Disease. Curr. Opin. Chem. Biol 2020, 55, 9–18. [PubMed: 31869674]

(34). Santo-Domingo J; Vay L; Hernández-SanMiguel E; Lobatón CD; Moreno A; Montero M; Alvarez J The Plasma Membrane Na^{+}/Ca^{2+} Exchange Inhibitor KB-R7943 Is Also a Potent Inhibitor of the Mitochondrial Ca^{2+} Uniporter. Br. J. Pharmacol 2007, 151, 647–654. [PubMed: 17471180]

(35). Thu VT; Kim H-K; Long LT; Lee S-R; Hanh TM; Ko TH; Heo H-J; Kim N; Kim SH; Ko KS; Rhee BD; Han J NecroX-5 Prevents Hypoxia/Reoxygenation Injury by Inhibiting the Mitochondrial Calcium Uniporter. Cardiovasc. Res 2012, 94, 342–350. [PubMed: 22425903]

(36). Schwartz J; Holmuhamedov E; Zhang X; Lovelace GL; Smith CD; Lemasters JJ Minocycline and Doxycycline, but Not Other Tetracycline-Derived Compounds, Protect Liver Cells from Chemical Hypoxia and Ischemia/Reperfusion Injury by Inhibition of the Mitochondrial Calcium Uniporter. Toxicol. Appl. Pharmacol 2013, 273, 172–179. [PubMed: 24012766]

(37). Arduino DM; Wettmarshausen J; Vais H; Navas-Navarro P; Cheng Y; Leimpek A; Ma Z; Delrio-Lorenzo A; Giordano A; Garcia-Perez C; Médard G; Kuster B; García-Sancho J; Mokranjac D; Foskett JK; Alonso MT; Perocchi F Systematic Identification of MCU Modulators by Orthogonal Interspecies Chemical Screening. Mol. Cell 2017, 67, 711–723. [PubMed: 28820965]

(38). Kon N; Murakoshi M; Isobe A; Kagechika K; Miyoshi N; Nagayama T DS16570511 Is a Small-Molecule Inhibitor of the Mitochondrial Calcium Uniporter. Cell Death Discov. 2017, 3, 17045. [PubMed: 28725491]

(39). Di Marco G; Vallese F; Jourde B; Bergsdorf C; Sturlese M; De Mario A; Techer-Etienne V; Haasen D; Oberhauser B; Schleeger S; Minetti G; Moro S; Rizzuto R; De Stefani D; Fornaro M; Mammucari C A High-Throughput Screening Identifies MICU1 Targeting Compounds. Cell Rep. 2020, 30, 2321–2331. [PubMed: 32075766]

(40). De Mario A; Tosatto A; Hill JM; Kriston-Vizi J; Ketteler R; Reane DV; Cortopassi G; Szabadkai G; Rizzuto R; Mammucari C Identification and Functional Validation of FDA-Approved Positive and Negative Modulators of the Mitochondrial Calcium Uniporter. Cell Rep. 2021, 35, 109275. [PubMed: 34161774]

(41). Emerson J; Clarke MJ; Ying W-L; Sanadi DR The Component of "Ruthenium Red" Responsible for Inhibition of Mitochondrial Calcium Ion Transport. Spectra, Electrochemistry, and Aquation Kinetics. Crystal Structure of μ-O-$[(HCO_2)(NH_3)_4Ru]_2Cl_3$. J. Am. Chem. Soc 1993, 115, 11799–11805.

(42). Matlib MA; Zhou Z; Knight S; Ahmed S; Choi KM; Krause-Bauer J; Phillips R; Altschuld R; Katsube Y; Sperelakis N; Bers DM Oxygen-Bridged Dinuclear Ruthenium Amine Complex Specifically Inhibits Ca^{2+} Uptake into Mitochondria in Vitro and in Situ in Single Cardiac Myocytes. J. Biol. Chem 1998, 273, 10223–10231. [PubMed: 9553073]

(43). Unitt JF; Boden KL; Wallace AV; Ingall AH; Coombs ME; Ince F Novel Cobalt Complex Inhibitors of Mitochondrial Calcium Uptake. Bioorg. Med. Chem 1999, 7, 1891–1896. [PubMed: 10530937]

(44). Nathan SR; Pino NW; Arduino DM; Perocchi F; MacMillan SN; Wilson JJ Synthetic Methods for the Preparation of a Functional Analogue of Ru360, a Potent Inhibitor of Mitochondrial Calcium Uptake. Inorg. Chem 2017, 56, 3123–3126. [PubMed: 28244741]

(45). Woods JJ; Nemani N; Shanmughapriya S; Kumar A; Zhang M; Nathan SR; Thomas M; Carvalho E; Ramachandran K; Srikantan S; Stathopulos PB; Wilson JJ; Madesh M A Selective and Cell-Permeable Mitochondrial Calcium Uniporter (MCU) Inhibitor Preserves Mitochondrial Bioenergetics after Hypoxia/Reoxygenation Injury. ACS Cent. Sci 2019, 5, 153–166. [PubMed: 30693334]

(46). Woods JJ; Rodriguez MX; Tsai C-W; Tsai M-F; Wilson JJ Cobalt Amine Complexes and Ru265 Interact with the DIME Region of the Mitochondrial Calcium Uniporter. Chem. Commun 2021, 57, 6161–6164.

(47). Cervinka J; Gobbo A; Biancalana L; Markova L; Novohradsky V; Guelfi M; Zacchini S; Kasparkova J; Brabec V; Marchetti F Ruthenium(II)−Tris-Pyrazolylmethane Complexes Inhibit Cancer Cell Growth by Disrupting Mitochondrial Calcium Homeostasis. J. Med. Chem 2022, 65, 10567–10587. [PubMed: 35913426]

(48). Moore CL Specific Inhibition of Mitochondrial Ca^{++} Transport by Ruthenium Red. Biochem. Biophys. Res. Commun 1971, 42, 298–305. [PubMed: 4250976]

(49). Broekemeier KM; Krebsbach RJ; Pfeiffer DR Inhibition of the Mitochondrial Ca^{2+} Uniporter by Pure and Impure Ruthenium Red. Mol. Cell. Biochem 1994, 139, 33–40. [PubMed: 7531818]

(50). Ying W-L; Emerson J; Clarke MJ; Sanadi DR Inhibition of Mitochondrial Calcium Ion Transport by an Oxo-Bridged Dinuclear Ruthenium Ammine Complex. Biochemistry 1991, 30, 4949–4952. [PubMed: 2036363]

(51). Woods JJ; Lovett J; Lai B; Harris HH; Wilson JJ Redox Stability Controls the Cellular Uptake and Activity of Ruthenium-Based Inhibitors of the Mitochondrial Calcium Uniporter (MCU). Angew. Chem., Int. Ed 2020, 59, 6482–6491.

(52). Novorolsky RJ; Nichols M; Kim JS; Pavlov EV; Woods JJ; Wilson JJ; Robertson GS The Cell-Permeable Mitochondrial Calcium Uniporter Inhibitor Ru265 Preserves Cortical Neuron Respiration after Lethal Oxygen Glucose Deprivation and Reduces Hypoxic/Ischemic Brain Injury. J. Cereb. Blood Flow Metab 2020, 40, 1172–1181. [PubMed: 32126877]

(53). Woods JJ; Spivey JA; Wilson JJA [1H,15N] Heteronuclear Single Quantum Coherence NMR Study of the Solution Reactivity of the Ruthenium-Based Mitochondrial Calcium Uniporter Inhibitor Ru265. Eur. J. Inorg. Chem 2022, 2022, e202100995.

(54). Testa B; Crivori P; Reist M; Carrupt P-A The Influence of Lipophilicity on the Pharmacokinetic Behavior of Drugs: Concepts and Examples. Perspect. Drug Discov. Des 2000, 19, 179–211.

(55). Leeson PD; Davis AM Time-Related Differences in the Physical Property Profiles of Oral Drugs. J. Med. Chem 2004, 47, 6338–6348. [PubMed: 15566303]

(56). Leeson PD; Springthorpe B The Influence of Drug-like Concepts on Decision-Making in Medicinal Chemistry. Nat. Rev. Drug Discov 2007, 6, 881–890. [PubMed: 17971784]

(57). Hughes JD; Blagg J; Price DA; Bailey S; DeCrescenzo GA; Devraj RV; Ellsworth E; Fobian YM; Gibbs ME; Gilles RW; Greene N; Huang E; Krieger-Burke T; Loesel J; Wager T; Whiteley L; Zhang Y Physiochemical Drug Properties Associated with in Vivo Toxicological Outcomes. Bioorg.Med.Chem.Lett 2008, 18, 4872–4875. [PubMed: 18691886]

(58). Waring MJ Defining Optimum Lipophilicity and Molecular Weight Ranges for Drug Candidates-Molecular Weight Dependent Lower Log*D* Limits Based on Permeability. Bioorg.Med.Chem.Lett 2009, 19, 2844–2851. [PubMed: 19361989]

(59). Gleeson MP; Hersey A; Montanari D; Overington J Probing the Links between in Vitro Potency, ADMET and Physicochemical Parameters. Nat. Rev. Drug Discov 2011, 10, 197–208. [PubMed: 21358739]

(60). Liu X; Testa B; Fahr A Lipophilicity and Its Relationship with Passive Drug Permeation. Pharm. Res 2011, 28, 962–977. [PubMed: 21052797]

(61). Johnson TW; Gallego RA; Edwards MP Lipophilic Efficiency as an Important Metric in Drug Design. J. Med. Chem 2018, 61, 6401–6420. [PubMed: 29589935]

(62). Johnstone TC; Lippard SJ The Effect of Ligand Lipophilicity on the Nanoparticle Encapsulation of Pt(IV) Prodrugs. Inorg. Chem 2013, 52, 9915–9920. [PubMed: 23859129]

(63). Zheng Y-R; Suntharalingam K; Johnstone TC; Yoo H; Lin W; Brooks JG; Lippard SJ Pt(IV) Prodrugs Designed to Bind Non-Covalently to Human Serum Albumin for Drug Delivery. J. Am. Chem. Soc 2014, 136, 8790–8798. [PubMed: 24902769]

(64). Awuah SG; Zheng Y-R; Bruno PM; Hemann MT; Lippard SJ A Pt(IV) Pro-Drug Preferentially Targets Indoleamine-2,3-Dioxygenase, Providing Enhanced Ovarian Cancer Immuno-Chemotherapy. J. Am. Chem. Soc 2015, 137, 14854–14857. [PubMed: 26561720]

(65). Ammar AA; Raveendran R; Gibson D; Nassar T; Benita S A Lipophilic Pt(IV) Oxaliplatin Derivative Enhances Antitumor Activity. J. Med. Chem 2016, 59, 9035–9046. [PubMed: 27603506]

(66). Hallett AJ; Placet E; Prieux R; McCafferty D; Platts JA; Lloyd D; Isaacs M; Hayes AJ; Coles SJ; Pitak MB; Marchant S; Marriott SN; Allemann RK; Dervisi A; Fallis IA Exploring the Cellular Uptake and Localisation of Phosphorescent Rhenium: Fac-Tricarbonyl Metallosurfactants as a Function of Lipophilicity. Dalton Trans. 2018, 47, 14241–14253. [PubMed: 29789819]

(67). Konkankit CC; Vaughn BA; Huang Z; Boros E; Wilson JJ Systematically Altering the Lipophilicity of Rhenium(I) Tricarbonyl Anticancer Agents to Tune the Rate at Which They Induce Cell Death. Dalton Trans. 2020, 49, 16062–16066. [PubMed: 32319485]

(68). Johnston DH; Shriver DF Vibrational Study of the Trifluoromethanesulfonate Anion: Unambiguous Assignment of the Asymmetric Stretching Modes. Inorg. Chem 1993, 32, 1045–1047.

(69). Parsons S; Clegg W Crystal Structure Analysis Principles and Practice. In Crystal Structure Analysis Principles and Practice; Oxford University Press: New York, NY, 2009; p 211.

(70). Matteoli U; Menchi G; Bianchi M; Piacenti F; Ianelli S; Nardelli M Structure and Catalytic Activity of Phosphine-Substituted Ruthenium Carbonyl Carboxylates. J. Organomet. Chem 1995, 498, 177–186.

(71). Malik KZ; Robinson SD; Steed JW Ruthenium Carboxylate Complexes $[Ru(O_2CR)_2(H_2O)(Me_2SO)_3]$ (R = Me, CF_3)-Synthesis and X-Ray Crystal Structures. Polyhedron 2000, 19, 1589–1592.

(72). Hiett NP; Lynam JM; Welby CE; Whitwood AC Ruthenium Carboxylate Complexes as Easily Prepared and Efficient Catalysts for the Synthesis of β-Oxopropyl Esters. J. Organomet. Chem 2011, 696, 378–387.

(73). Carmona D; Viguri F; Lamata MP; Ferrer J; Bardají E; Lahoz FJ; García-Orduña P; Oro LA Ruthenium Amino Carboxylate Complexes as Asymmetric Hydrogen Transfer Catalysts. Dalton Trans. 2012, 41, 10298–10308. [PubMed: 22825563]

(74). Jeschke J; Gäbler C; Korb M; Rüffer T; Lang H Ruthenium Carboxylate Complexes as Efficient Catalysts for the Addition of Carboxylic Acids to Propargylic Alcohols. Eur. J. Inorg. Chem 2015, 2015, 2939–2947.

(75). Wilson JJ; Lippard SJ Synthesis, Characterization, and Cytotoxicity of Platinum(IV) Carbamate Complexes. Inorg. Chem 2011, 50, 3103–3115. [PubMed: 21361279]

(76). Gellene GI Application of Kinetic Approximations to the A ⇄ B → C Reaction System. J. Chem. Educ 1995, 72, 196–199.

(77). Verhaagh S; Schweifer N; Barlow DP; Zwart R Cloning of the Mouse and Human Solute Carrier 22a3 (Slc22a3/SLC22A3) Identifies a Conserved Cluster of Three Organic Cation Transporters on Mouse Chromosome 17 and Human 6q26–Q27. Genomics 1999, 55, 209–218. [PubMed: 9933568]

(78). Gründemann D; Schechinger B; Rappold GA; Schömig E Molecular Identification of the Corticosterone-Sensitive Extraneuronal Catecholamine Transporter. Nat. Neurosci 1998, 1, 349–351. [PubMed: 10196521]

(79). Koepsell H; Lips K; Volk C Polyspecific Organic Cation Transporters: Structure, Function, Physiological Roles, and Biopharmaceutical Implications. Pharm. Res 2007, 24, 1227–1251. [PubMed: 17473959]

(80). Ogasawara M; Yamauchi K; Satoh Y-I; Yamaji R; Inui K; Jonker JW; Schinkel AH; Maeyama K Recent Advances in Molecular Pharmacology of the Histamine Systems: Organic Cation Transporters as a Histamine Transporter and Histamine Metabolism. J. Pharmacol. Sci 2006, 101, 24–30. [PubMed: 16648665]

(81). Phillips C Fluorophore-Based Mitochondrial Ca^{2+} Uptake Assay. Bio-protocol 2018, 8, e2934. [PubMed: 34395755]

(82). Urgiles J; Nathan SR; MacMillan SN; Wilson JJ Dinuclear Nitrido-Bridged Ruthenium Complexes Bearing Diimine Ligands. Dalton Trans. 2017, 46, 14256–14263. [PubMed: 28994442]

(83). Sheldrick GM A Short History of SHELX. Acta Crystallogr. Sect. A Found. Crystallogr 2008, 64, 112–122.

(84). Sheldrick GM Crystal Structure Refinement with SHELXL. Acta Crystallogr. Sect. C Struct. Chem 2015, 71, 3–8. [PubMed: 25567568]

(85). Müller P Practical Suggestions for Better Crystal Structures. Crystallogr. Rev 2009, 15, 57–83.

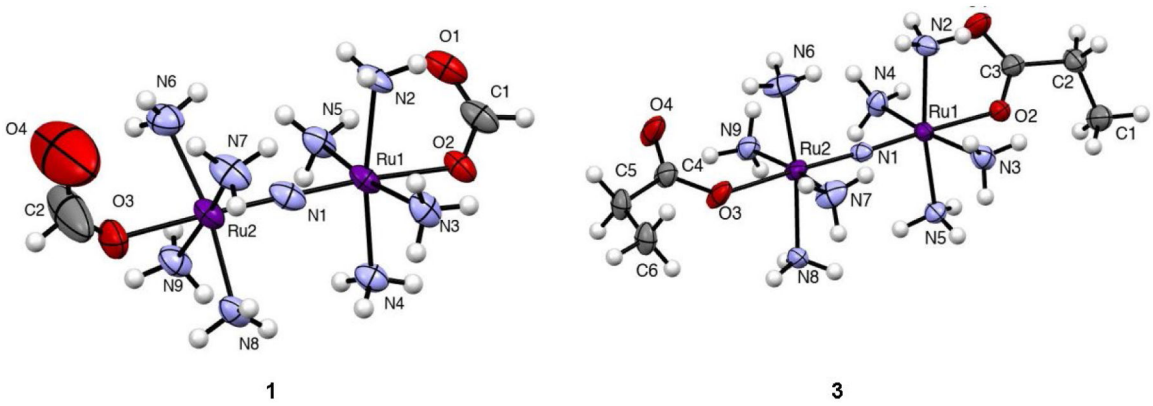

Figure 1.

The crystal structures of **1** and **3**. Outer-sphere ions and solvent molecules are omitted for clarity. Thermal ellipsoids are shown at the 50% probability level. For **1**, only one of the two complex cations present in the asymmetric unit is shown. The other complex cation is shown in Figure S26 within the SI. Crystallographic information for both complexes are given in Table 1. Interatomic distances and angles are given in Table 2.

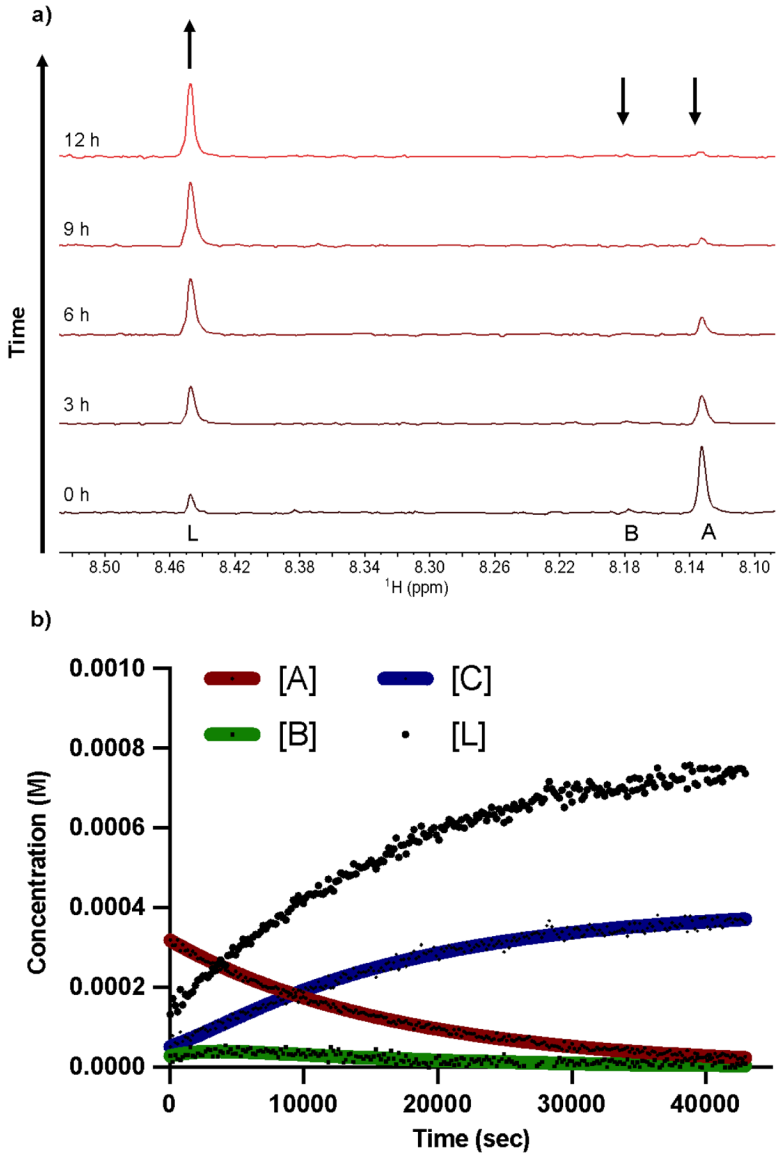

Figure 2.

Representative kinetic analysis of **1** at 37 °C via ^{1}H NMR spectroscopy in pH 7.4 MOPS-buffered solution containing 10% D_2O and <1% *p*-dioxane as a chemical shift reference. a) The proton resonances of each species **A**, **B**, and **L** are shown, and b) the relative concentration of each species is plotted over time to calculate the rate constants k_1 and k_2. Analyses for **2**, **3**, and **4** can be found in the SI (Figures S15–17).

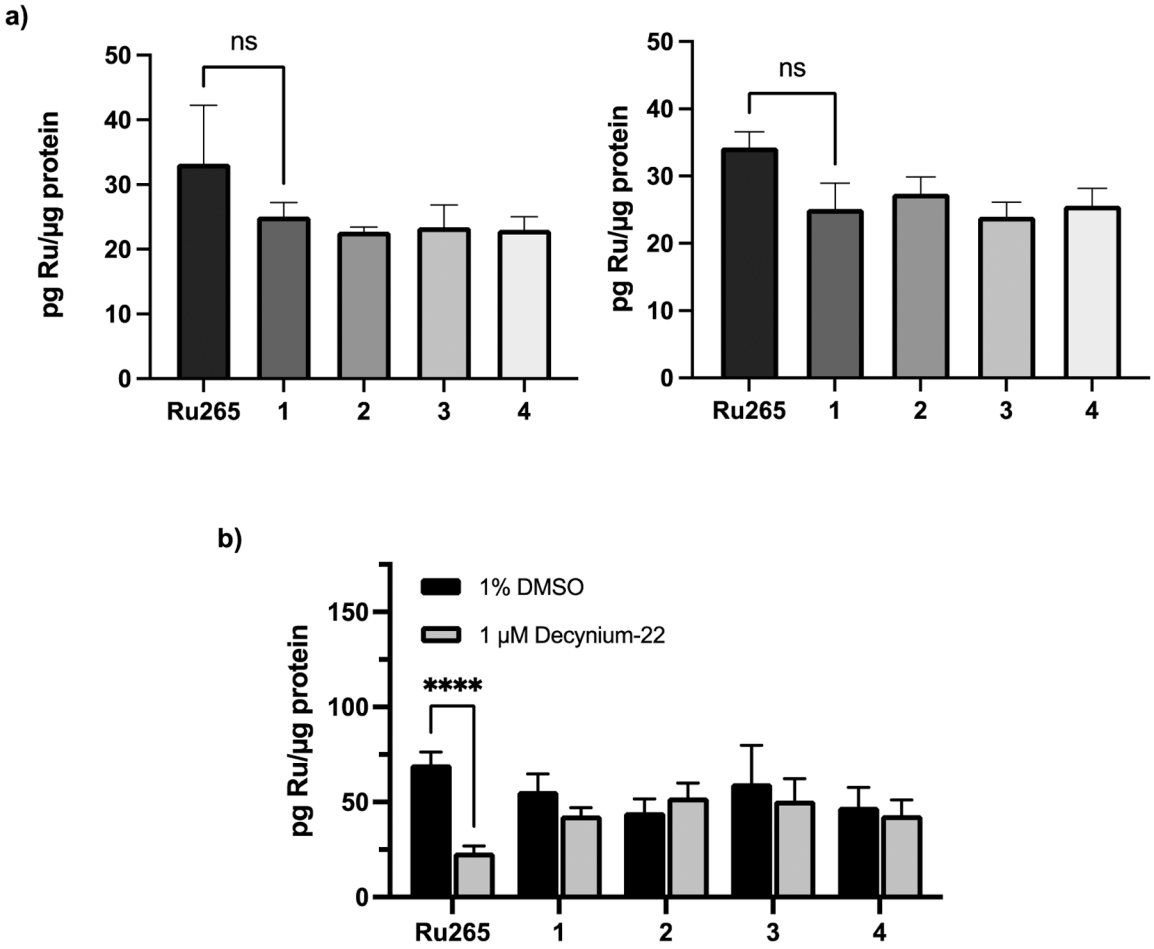

Figure 3.

a) Cellular uptake of Ru265, **1**, **2**, **3**, and **4** in HeLa (left) and HEK293T (right) cells after incubating the cells with 50 μM of the compound for 2 h. b) Cellular uptake of Ru265, **1**, **2**, **3**, and **4** in HeLa cells in the presence and absence of the OCT3 inhibitor decynium-22 after incubating the cells with 50 μM of the compound for 3 h. Data are represented as the mean uptake ± SD; ****$p < 0.005$; ns = not significant; n = 3.

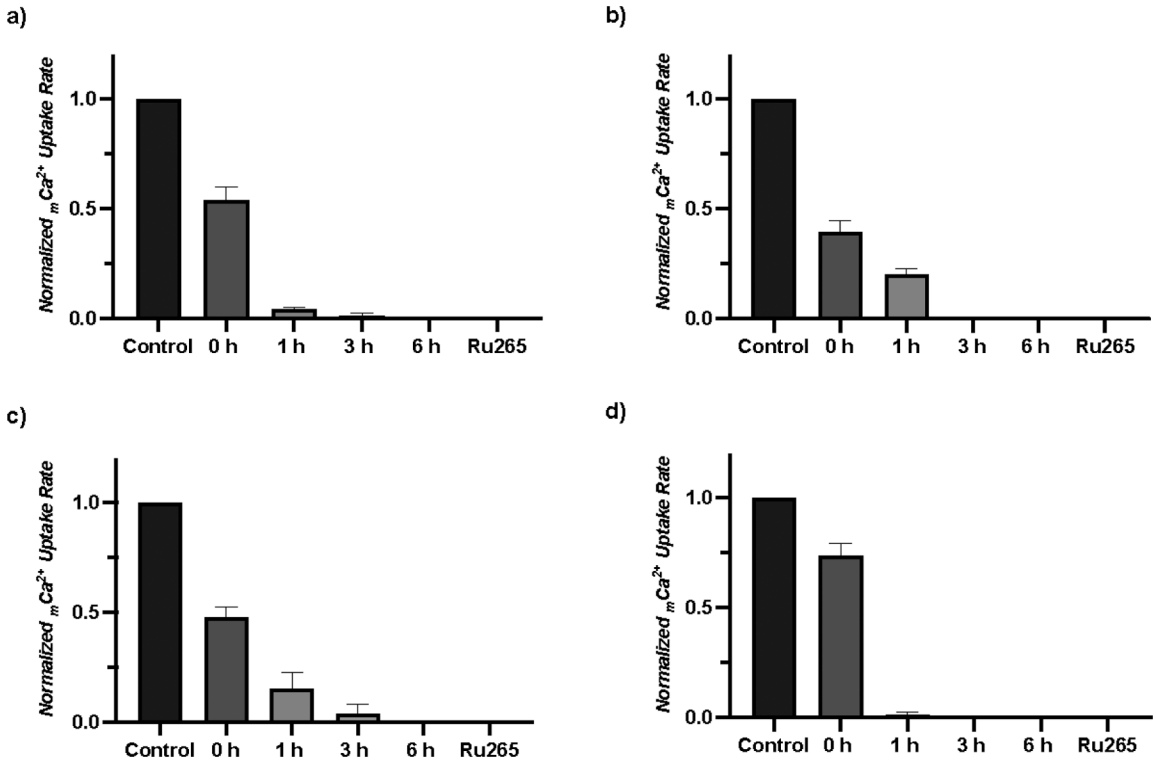

Figure 4.

Time-dependent mitochondrial Ca^{2+} uptake rates of 10 nM solutions of a) **1**, b) **2**, c) **3**, and d) **4** in pH 7.4 MOPS-buffered solution in permeabilized HEK293T cells (1×10^7 cells mL^{-1}). Each time point was prepared from a 400 μM stock of the complexes incubated in 40 mM MOPS-buffered solution (pH 7.4) and diluted to 10 nM in 18 MΩ·cm H_2O at the time of the experiment. All uptake rates were normalized to the rate of untreated (control) cells.

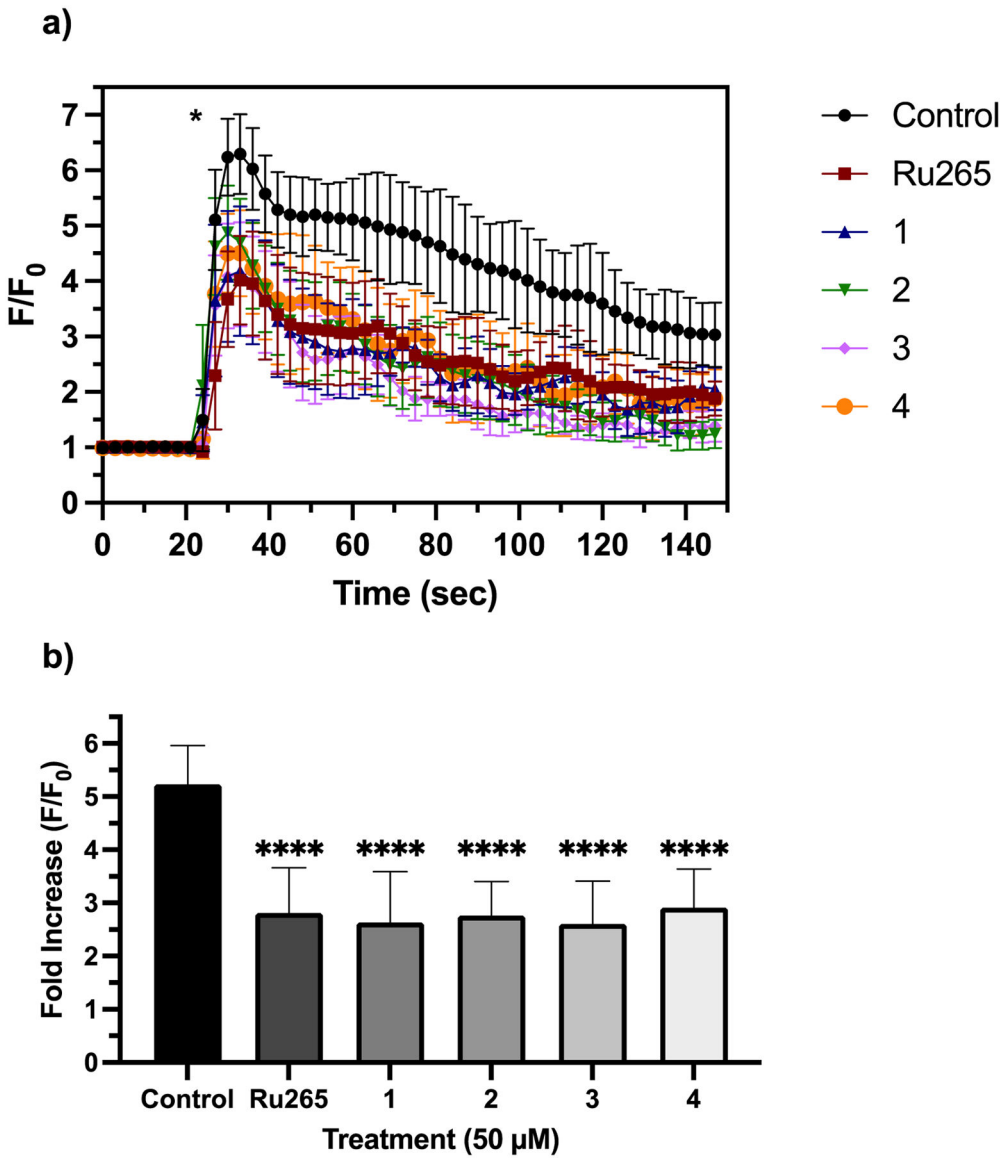

Figure 5.

a) Mitochondrial Ca^{2+} transients in HeLa cells after treatment with histamine (100 μM), indicated with an asterisk (*), that were pretreated with or without Ru265, **1**, **2**, **3**, or **4** (50 μM) for 1 h. Data are presented as the mean response ± SD. b) Fold increase (F/F_0) of the fluorescence response of each treatment upon addition of histamine (100 μM). Data are presented as the mean response ± SD. ****$p < 0.005$; $n = 6$.

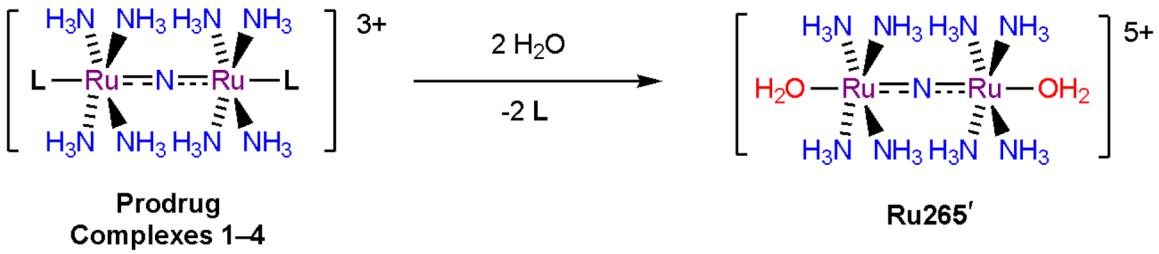

Prodrug Complexes 1–4 **Ru265′**

Scheme 1.

Strategy to develop prodrugs for Ru265′ through aquation of the axial ligands.

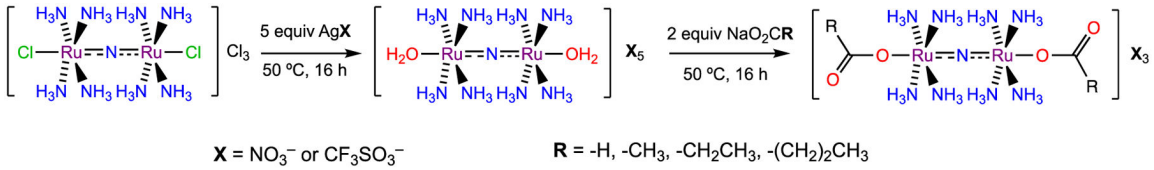

Scheme 2.

Synthetic scheme for compounds **1**, **2**, **3**, and **4**. Compounds **1**, **2**, and **3** were synthesized as nitrate salts, whereas compound **4** was synthesized as a triflate salt.

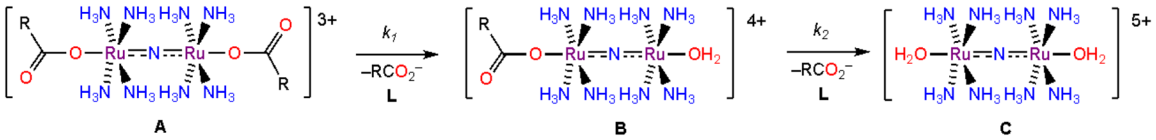

Scheme 3.

The aquation pathway of the carboxylate-functionalized compounds.

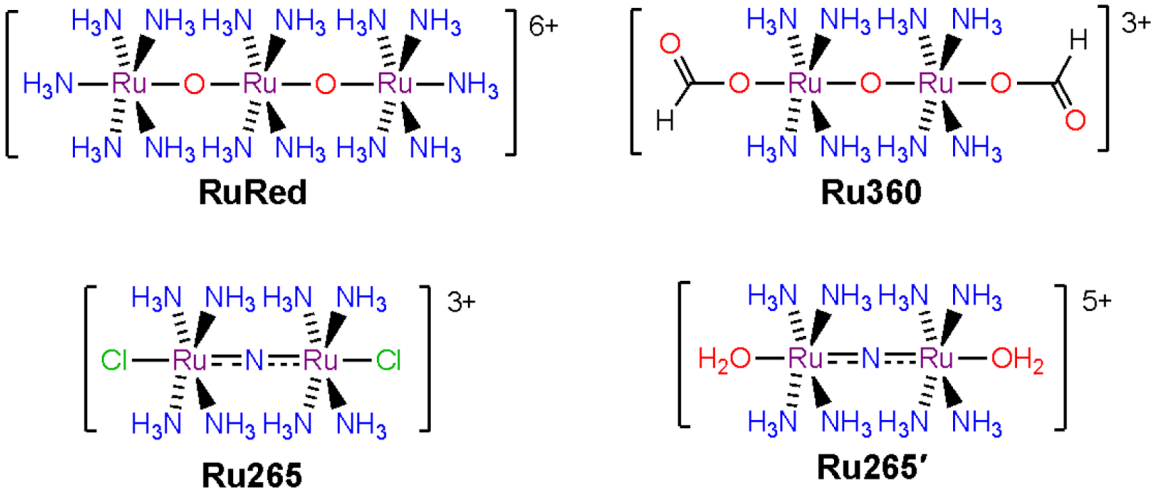

Chart 1.
Structures of Ru-based MCU inhibitors.

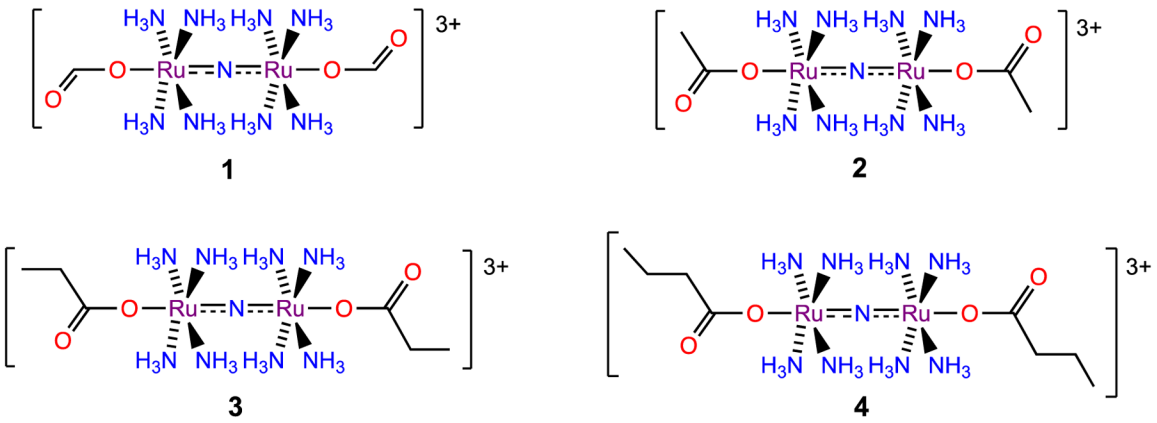

Chart 2.
Structures of compounds discussed in this work.

Table 1.

X-ray crystal data and structure refinement details for **1** and **3**.

Compound	**1·3MeOH**	**3·H_2O**
Empirical Formula	$C_6H_{29}F_9N_9O_{14}Ru_2S_3$	$C_6H_{36}N_{12}O_{14}Ru_2$
Formula Weight	920.70	702.57
a (Å)	25.0552(2)	10.41150(10)
b (Å)	10.35730(10)	12.02830(10)
c (Å)	24.9114(3)	20.3198(2)
α (°)	90	90
β (°)	100.8730(10)	104.6280(10)
γ (°)	90	90
V (Å^3)	6348.56(11)	2462.22(4)
Z	8	4
Crystal System	Monoclinic	Monoclinic
Space Group	$P2_1/c$	$P2_1/n$
ρ_{calc} (Mg/m^3)	1.927	1.895
μ (Cu Kα), mm^{-1}	10.681	
μ (Mo Kα), mm^{-1}		1.310
λ, Å	1.54184	0.7073
T (K)	100.0(8)	100.00(10)
2θ range (°)	3.593 – 77.525	2.072 – 26.022
Independent Reflections	27170	4846
R_{int}	0.079	0.0286
Number of Parameters	795	482
Largest diff. peak and hole (Å^{-3})	2.203/−2.018	1.717/−0.737
GoF	1.041	1.165
R1/wR2 (all data)	0.0896/0.2330	0.0343/0.0866
R1/wR2 (I >2σ)	0.0820/0.2260	0.0333/0.0860

Cu Kα λ = 1.54184 Å; Mo Kα λ = 0.7073 Å

$R_1 = \Sigma||F_O|-|F_C||/\Sigma|F_O|$; $wR2 = \{\Sigma[w(F_O^2-F_C^2)^2]/\Sigma([F_O^2)^2]\}^{1/2}$

GoF = $\{\Sigma[w(F_O^2-F_C^2)^2]/(n-p)\}^{1/2}$, where n is the number of data and p is the number of refined parameters

Table 2.

Selected interatomic distances and angles for **1** and **3**.

Selected Interatomic Distances (Å) for 1·3MeOH				**Selected Interatomic Distances (Å) for 3·H_2O**			
Ru(1)–O(2)	2.110(6)	Ru(2)–O(3)	2.080(8)	Ru(1)–O(2)	2.076(2)	Ru(2)–O(3)	2.082(3)
Ru(1)–N(1)	1.756(9)	Ru(2)–N(1)	1.730(9)	Ru(1)–N(1)	1.745(3)	Ru(2)–N(1)	1.743(3)
Ru(1)–N(2)	2.105(7)	Ru(2)–N(6)	2.117(9)	Ru(1)–N(2)	2.119(3)	Ru(2)–N(6)	2.114(3)
Ru(1)–N(3)	2.110(7)	Ru(2)–N(7)	2.122(8)	Ru(1)–N(3)	2.115(3)	Ru(2)–N(7)	2.115(4)
Ru(1)–N(4)	2.107(8)	Ru(2)–N(8)	2.107(8)	Ru(1)–N(4)	2.089(3)	Ru(2)–N(8)	2.100(3)
Ru(1)–N(5)	2.122(7)	Ru(2)–N(9)	2.117(8)	Ru(1)–N(5)	2.096(3)	Ru(2)–N(9)	2.098(3)
Selected Interatomic Angles (°) for 1				**Selected Interatomic Angles (°) for 3**			
N(1)–Ru(1)–O(2)	175.9(3)	N(1)–Ru(2)–O(3)	176.0(4)	N(1)–Ru(1)–O(2)	177.49(12)	N(1)–Ru(2)–O(3)	177.65(12)
N(1)–Ru(1)–N(2)	96.1(4)	N(1)–Ru(2)–N(6)	94.6(4)	N(1)–Ru(1)–N(2)	95.28(12)	N(1)–Ru(2)–N(6)	94.64(14)
N(1)–Ru(1)–N(3)	95.0(3)	N(1)–Ru(2)–N(7)	96.0(4)	N(1)–Ru(1)–N(3)	95.96(13)	N(1)–Ru(2)–N(7)	96.57(14)
N(1)–Ru(1)–N(4)	93.4(3)	N(1)–Ru(2)–N(8)	96.0(4)	N(1)–Ru(1)–N(4)	93.08(13)	N(1)–Ru(2)–N(8)	95.27(12)
N(1)–Ru(1)–N(5)	93.8(3)	N(1)–Ru(2)–N(9)	92.3(3)	N(1)–Ru(1)–N(5)	95.09(12)	N(1)–Ru(2)–N(9)	92.64(13)
N(2)–Ru(1)–N(3)	87.3(3)	N(6)-Ru(2)–N(7)	89.7(4)	N(2)–Ru(1)–N(3)	89.92(13)	N(6)-Ru(2)–N(7)	89.33(14)
N(2)–Ru(1)–N(4)	170.4(3)	N(6)–Ru(2)–N(8)	169.5(4)	N(2)–Ru(1)–N(4)	89.95(13)	N(6)–Ru(2)–N(8)	170.05(14)
N(2)–Ru(1)–N(5)	90.0(3)	N(6)–Ru(2)–N(9)	91.4(4)	N(2)–Ru(1)–N(5)	169.61(12)	N(6)–Ru(2)–N(9)	89.48(14)
N(2)–Ru(1)–O(2)	87.2(3)	N(6)–Ru(2)–O(3)	85.9(4)	N(2)–Ru(1)–O(2)	86.50(11)	N(6)–Ru(2)–O(3)	87.40(14)
N(3)–Ru(1)–N(4)	90.7(3)	N(7)–Ru(2)–N(8)	89.8(4)	N(3)–Ru(1)–N(4)	170.94(12)	N(7)–Ru(2)–N(8)	88.62(13)
N(3)–Ru(1)–N(5)	171.0(3)	N(7)–Ru(2)–N(9)	171.6(4)	N(3)–Ru(1)–N(5)	89.51(12)	N(7)–Ru(2)–N(9)	170.78(13)
N(3)–Ru(1)–O(2)	82.8(3)	N(7)–Ru(2)–O(3)	88.0(4)	N(3)–Ru(1)–O(2)	82.25(11)	N(7)–Ru(2)–O(3)	82.27(13)
N(4)–Ru(1)–N(5)	90.6(3)	N(8)–Ru(2)–N(9)	87.6(3)	N(4)–Ru(1)–N(5)	88.99(12)	N(8)–Ru(2)–N(9)	90.98(13)
N(4)–Ru(1)–O(2)	83.2(3)	N(8)–Ru(2)–O(3)	83.5(4)	N(4)–Ru(1)–O(2)	88.70(11)	N(8)–Ru(2)–O(3)	82.68(12)
N(5)–Ru(1)–O(2)	88.5(3)	N(9)–Ru(2)–O(3)	83.7(4)	N(5)–Ru(1)–O(2)	83.15(11)	N(9)–Ru(2)–O(3)	88.53(12)
Ru(1)–N(1)–Ru(2)	176.5(5)			Ru(1)–N(1)–Ru(2)	175.43(19)		

Atoms are labelled as shown in Figure 1. Values in parentheses indicate the standard uncertainty in the last significant figure.

Compound **1** contains two molecules in the asymmetric unit. Data shown are from one of these two molecules. Interatomic distances and angles are similar between the two molecules. Data for the second molecule are shown in the SI (Table S1 and Figure S26).

Table 3.

Aquation rate constants (k_1 and k_2) and half-lives ($t_{1/2}$) of Ru265 and compounds **1**–**4** at 37 °C. The pK_a values of the conjugate acid of the free ligands are also given.

Complex	$k_1 \times 10^5$ (s^{-1})	$t_{1/2\,(1)}$ (h)	$k_2 \times 10^4$ (s^{-1})	$t_{1/2\,(2)}$ (h)	pK_a (HL)
Ru265 [a]	49.2	0.038	–	–	5.90
1	5.9 ± 0.2	3.3 ± 0.1	3.6 ± 0.3	0.50 ± 0.05	3.75
2	2.0 ± 0.5	9.9 ± 2.4	3.0 ± 1.2	0.7 ± 0.3	4.75
3	2.8 ± 0.1	6.9 ± 0.2	3.3 ± 0.5	0.6 ± 0.1	4.88
4	3.2 ± 0.1	5.9 ± 0.2	2.8 ± 0.2	0.700 ± 0.004	4.82

[a] Reference 51. The rate constant was determined using UV-vis spectroscopy and was only able to resolve the first aquation step.

Table 4.

IC_{50} values of MCU-mediated $_{m}Ca^{2+}$ uptake inhibition for Ru265 and derivatives in permeabilized HEK293T cells (1×10^7 cells/mL).

Complex	IC_{50} (nM)
Ru265[a]	8.6 ± 2.2
1	14.7 ± 2.9
2	18.8 ± 1.2
3	19.1 ± 1.7
4	18.7 ± 0.1

[a]Reference 46